Chemical Geology 573 (2021) 120200

Contents lists available at ScienceDirect

Chemical Geology

journal homepage: www.elsevier.com/locate/chemgeo

Experimental and modeling studies of PR and ND oxalate solubility to high ionic strengths: Insight into actinide(III) oxalates

Yongliang Xiong *, Yifeng Wang

Sandia National Laboratories (SNL), Nuclear Waste Disposal Research & Analysis, 1515 Eubank Boulevard SE, Albuquerque, NM 87123, USA

ARTICLE INFO

Editor: Karen Johannesson

Keywords:
Geological disposal of nuclear waste
Mobility of rare earth elements (REE)
Pitzer model
Separation of actinides in reprocessing
Extraction of rare earth elements (REE)

ABSTRACT

Actinide oxalates are chemical compounds important to nuclear industry, ranging from actinide separation in waste reprocessing, to production of specialty actinides, and to disposal of high level nuclear waste (HLW) and spent nuclear fuel (SNF). In this study, the solubility constants for $Pr_2(C_2O_4)_3{\cdot}10H_2O$ and $Nd_2(C_2O_4)_3{\cdot}10H_2O$ by performing solubility experiments in HNO_3 and mixtures of HNO_3 and $H_2C_2O_4$ at $23.0 \pm 0.2\,^{\circ}C$ have been determined. The targeted starting materials, $Pr_2(C_2O_4)_3{\cdot}10H_2O$ and $Nd_2(C_2O_4)_3{\cdot}10H_2O$, were successfully synthesized at room temperature using $PrCl_3$, $NdCl_3$ and oxalic acid as the source metrials. Then, we utilized the targeted solubility-controlling phases to conduct solubility measurements. There was no phase change over the entire periods of experiments, demonstrating that $Pr_2(C_2O_4)_3{\cdot}10H_2O$ and $Nd_2(C_2O_4)_3{\cdot}10H_2O$ were the solubility-controlling phases in our respective experiments.

Based on our experimental data, we have developed a thermodynamic model for $Pr_2(C_2O_4)_3{\cdot}10H_2O$ and $Nd_2(C_2O_4)_3{\cdot}10H_2O$ in the mixtures of HNO_3 and $H_2C_2O_4$ to high ionic strengths. The model for $Pr_2(C_2O_4)_3{\cdot}10H_2O$ reproduces well the reported experimental data for $Pu_2(C_2O_4)_3{\cdot}10H_2O$, which are not utilized for the model development, demonstrating that Pr(III) is an excellent analog for Pu(III). Similarly, the model for $Nd_2(C_2O_4)_3{\cdot}10H_2O$ reproduces the solubility of $Am_2(C_2O_4)_3{\cdot}10H_2O$ and $Cm_2(C_2O_4)_3{\cdot}10H_2O$. The Pitzer model was used for the calculation of activity coefficients. Based on the published, well established model for dissociation constants for oxalic acid and stability constants for actinide-oxalate complexes [i.e., $AmC_2O_4^+$, and $Am(C_2O_4)_2^-$] to high ionic strengths, we have obtained the solubility constants ($\log_{10}K^0$) for the following reactions at 25 °C,

$$Pr_2(C_2O_4)_3{\cdot}10H_2O \rightleftharpoons 2Pr^{3+} + 3C_2O_4^{2-} + 10H_2O(l)$$
$$Nd_2(C_2O_4)_3{\cdot}10H_2O \rightleftharpoons 2Nd^{3+} + 3C_2O_4^{2-} + 10H_2O(l)$$

to be -30.82 ± 0.30 (2σ), and -31.14 ± 0.35 (2σ), respectively. These values can be directly applied to $Pu_2(C_2O_4)_3{\cdot}10H_2O$, $Am_2(C_2O_4)_3{\cdot}10H_2O$ and $Cm_2(C_2O_4)_3{\cdot}10H_2O$.

The model established for actinide oxalates by this study provides the needed knowledge with regard to solubilities of actinide/REE oxalates at various ionic strengths, and is expected to find applications in many fields, including the geological disposal of nuclear waste and the mobility of REE under the surface conditions, as $Pr_2(C_2O_4)_3{\cdot}10H_2O$ and $Nd_2(C_2O_4)_3{\cdot}10H_2O$ can be regarded as the pure Pr and Nd end-members of deveroite, a recently discovered natural REE oxalate with the following stoichiometry, $(Ce_{1.01}Nd_{0.33}La_{0.32}Pr_{0.11}Y_{0.11}Sm_{0.01}Pb_{0.04}U_{0.03}Th_{0.01}Ca_{0.04})_{2.01}(C_2O_4)_{2.99}{\cdot}9.99H_2O$. Regarding its importance in the geological disposal of nuclear waste, $Am_2(C_2O_4)_3{\cdot}10H_2O$/$Pu_2(C_2O_4)_3{\cdot}10H_2O$/$Cm_2(C_2O_4)_3{\cdot}10H_2O$ can be the source-term phase for actinides, as demonstrated by the instance in the disposal in clay/shale formations. This is exemplified by the stability of $Am_2(C_2O_4)_3{\cdot}10H_2O$ in comparison with $Am(OH)_3$(am), $Am(OH)_3$(s) and $AmCO_3(OH)$(s) under the relevant geological repository conditions.

* Corresponding author.
E-mail address: yxiong@sandia.gov (Y. Xiong).

https://doi.org/10.1016/j.chemgeo.2021.120200
Received 29 January 2021; Received in revised form 22 March 2021; Accepted 24 March 2021
Available online 31 March 2021
0009-2541/© 2021 Elsevier B.V. All rights reserved.

1. Introduction

Actinide oxalates are a family of chemical compounds important for nuclear industry. In the nuclear fuel cycle, long-lived and alpha-emitting actinides with high radiotoxicity are usually separated from other radioactive elements, as solid oxalate compounds for subsequent disposal, transmutation or purification for reuse. Their technological applications include (1) the usage of separated ^{238}Pu and ^{241}Am as radioisotope thermoelectric generators (RTGs) for space programs (Campbell et al., 2016); (2) the usage of co-separated Pu and U for manufacturing mixed oxide (MOX) fuel (Doty and Chong, 1970); (3) the use of ^{248}Cm as a target nuclide for creating new superheavy elements in accelerator studies (e.g., Hoffman, 1985; Lobanov et al., 1997; Tsyganov, 2014; Dmitriev and Popeko, 2015); and (4) the utilization of uranyl oxalate as a chemical actinometer (e.g., Leighton and Forbes, 1930).

In the field of nuclear waste management, organic ligands are expected to be present in various disposal concepts (Marsac et al., 2017b), and actinides and oxalate could both be present in nuclear waste in geological repositories. This is because oxalic acid and oxalate salts are used in decontamination of nuclear facilities. For instance, an aqueous waste of Pu and Am can be decontaminated by stepwise precipitation of a Pu and Am oxalate first, and then a lead oxalate (Akatsu, 1982). Therefore, when such waste is disposed of in a geological repository, the interactions between actinides and oxalate are important for performance assessment (PA) in geological repositories for nuclear wastes. As an example, in the Waste Isolation Pilot Plant (WIPP), a U.S. DOE geological repository for defense-related transuranic (TRU) waste in the bedded salt formations in New Mexico, USA, the inventory of oxalate in waste was ~50 metric tons for the WIPP Compliance Application Re-Certification Performance Assessment Baseline Calculations in 2004 (CRA-2004PABC) (Crawford et al., 2006). The oxalate concentrations were 4.55×10^{-2} mol·dm^{-3} (Brush and Xiong, 2005). As actinide oxalates have low solubilities, actinide oxalates could form in geological repositories for non-heat generating transuranic waste such as the WIPP to become solubility-controlling phases for actinides in the source term in the near field.

In clay repositories in the French nuclear waste management programs, Altmann (2008) stated that certain types of nuclear waste "contain significant amounts of organic compounds or substances which will be released, either 'as is' or after modification by waste package environmental conditions…, into the solution present in the waste cell." Oxalate is a major product when organic compounds are degraded (Ferri et al., 2000). In addition, oxalic acid is widely utilized for obtaining oxides of different actinides in the reprocessing of SNF, by first precipitation of actinide oxalates, and then thermal conversion of actinide oxalates to actinide oxides (Sarsfield, 2015). For instance, in the AREVAs spent nuclear fuel recycling plant in La Hague, the main conversion route of elemental plutonium into its oxide is through oxalic conversion (Dollimore, 1987; Machuron-Mandard and Madic, 1996; Arab-Chapelet et al., 2007). When such liquid waste is conditioned for disposal, oxalate will be present. Therefore, by taking account for oxalate generated by degradation of organic compounds as well as the directly disposed oxalate waste together, significant amounts of oxalate are expected to be present in certain geological repositories for high level nuclear waste (HLW).

Furthermore, oxalate is stable up to 175 °C (Kettler et al., 1991, 1998), and is present in natural formation waters with concentrations ranging from 2 to 119 ppm (e.g., MacGowan and Surdam, 1988, 1990) and in oil-field waters with concentrations ranging from 3 to 494 ppm (MacGowan and Surdam, 1988, 1990). Therefore, oxalate is expected to be stable in geological repositories for heat-generating HLW, even in the near field of a geological repository. In the far field of a geological repository, as whewellite ($CaC_2O_4·H_2O$) is "one of the most important minerals within the surface veneer of our planet" (Stephens, 2012), actinides leaked from a breached geological repository can react with whewellite in the geosphere to fix actinides. Therefore, oxalate could impact the geochemical conditions for both the near-field and far-field of geological repositories.

It has established that Pu(III), Am(III), and Cm(III) usually form decahydrate oxalates at ambient temperatures, $Pu_2(C_2O_4)_3·10H_2O$, $Am_2(C_2O_4)_3·10H_2O$, and $Cm_2(C_2O_4)_3·10H_2O$ (Markin, 1958; Chackraburtty, 1963; Jenkins et al., 1965; Weigel and Ter Meer, 1967; Scherer and Fochler, 1968; Lumetta et al., 2008). The lanthanide decahydrate oxalates, e.g., $Nd_2(C_2O_4)_3·10H_2O$, are isostructural with these actinide decahydrate oxalates (Weigel and Ter Meer, 1967). As actinide oxalates are important to numerous fields, the knowledge of their solubilities at various ionic strengths is a key to the aqueous processes in which they are precipitated. However, in a recent review by Nuclear Energy Agency (NEA) (Hummel et al., 2005), it was not able to develop a model for actinide oxalates in +III oxidation state.

In this work, we have conducted solubility measurements on $Pr_2(C_2O_4)_3·10H_2O$ and $Nd_2(C_2O_4)_3·10H_2O$. We target $Pr_2(C_2O_4)_3·10H_2O$ as an analog to $Pu_2(C_2O_4)_3·10H_2O$, and $Nd_2(C_2O_4)_3·10H_2O$ as analog to $Am_2(C_2O_4)_3·10H_2O$ and $Cm_2(C_2O_4)_3·10H_2O$. This is based on the facts that the effective ionic radius of Pr(III) for six coordination number is almost identical to that of Pu(III) for the same coordination number (i.e., 0.99 Å for Pr(III) versus 1.00 Å for Pu(III)) (see Shannon, 1976), and that the effective ionic radius of Nd(III) for six coordination number is almost identical to those of Am(III) and Cm(III) for the same coordination number (i.e., 0.983 Å for Nd(III) versus 0.975 Å for Am(III) and 0.97 Å for Cm(III)) (see Shannon, 1976). According to the same criteria, Ce(IV) is also identified as an analog to Pu(IV) (Marsac et al., 2017a). Based on our experimental data we have developed a thermodynamic model for $Pr_2(C_2O_4)_3·10H_2O$ and $Nd_2(C_2O_4)_3·10H_2O$, which is also valid to Pu(III)-, Am(III)-, and Cm(III)-oxalates. This model provides the needed knowledge for solubilities of actinide oxalates at various ionic strengths. The model developed by this study is expected to find applications in many fields, including the description of the stability of actinide oxalates in the near and far fields of geological repositories, and the extraction and recovery of rare earth elements.

2. Experimental methods

In our experiments, first, the solubility-controlling phases, $Pr_2(C_2O_4)_3·10H_2O$ and $Nd_2(C_2O_4)_3·10H_2O$, for the solubility measurements, were synthesized. In the synthesis, the source for Pr(III) is $PrCl_3·7H_2O$ from GFS Chemicals, and the source for Nd(III) is $NdCl_3·6H_2O$ also from GFS Chemicals. The source for oxalate is solid oxalic acid ($H_2C_2O_4·2H_2O$) from Fisher Scientific. Before the synthesis, the following stock solutions were prepared with DI water with resistivity ≥18.3 megohm: 0.67 mol·dm^{-3} $PrCl_3$, 0.70 mol·dm^{-3} $NdCl_3$, and 0.18 mol·dm^{-3} $H_2C_2O_4$. In the synthesis of $Pr_2(C_2O_4)_3·10H_2O$, 100 mL of 0.18 mol·dm^{-3} $H_2C_2O_4$ is first placed into a 400 mL glass beaker at room temperature. Then, 0.67 mol·dm^{-3} $PrCl_3$ solution is dropwise added into the beaker, and 0.18 mol·dm^{-3} $H_2C_2O_4$ solution is also dropwise added onto the beaker, with a ratio of 1:2. The precipitation was instantaneous, and the precipitates were settled down at the bottom of the glass beaker. The precipitates are filtered out with vacuum filtration. The filtration apparatus set includes mainly a ceramic filter funnel, a borosilicate funnel support base, a borosilicate glass receiver-flask, and a vacuum pump. The smooth fluted Grade 313 filter papers from VWR® were used for the filtration. The filter paper has the following specifications: 12.5 cm in diameter and particle retention size of 5 μm. The filtered precipitates are dried at room temperature overnight. The synthetic $Pr_2(C_2O_4)_3·10H_2O$ has a light green color, like the color of pistachio. $Nd_2(C_2O_4)_3·10H_2O$ is synthesized using the same procedure except that 0.70 mol·dm^{-3} $NdCl_3$ solution is used instead of 0.67 mol·dm^{-3} $PrCl_3$ solution. The synthetic $Nd_2(C_2O_4)_3·10H_2O$ has a very light purple color.

In the solubility experiments, about 0.5–1.5 g of the starting material were weighed out and placed into 150 mL plastic bottles. Then, 100 mL of supporting electrolyte solutions were added to those bottles. Once

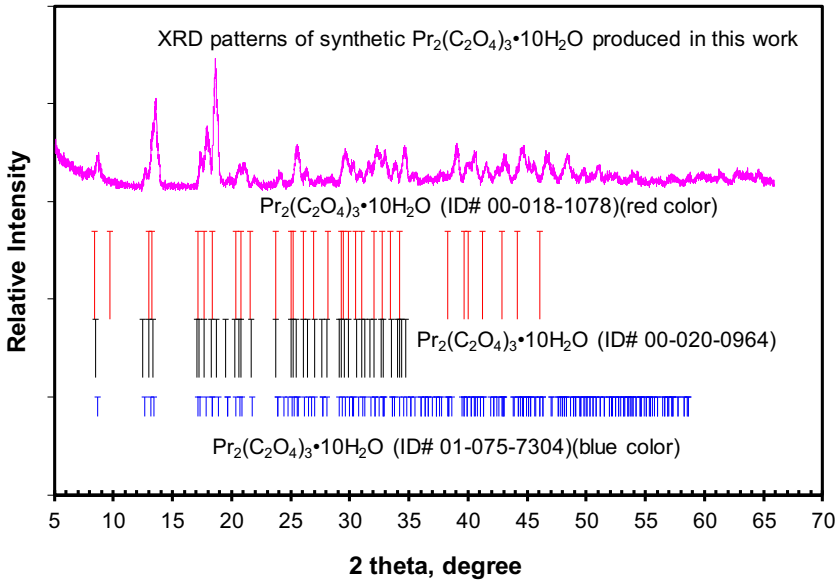


Fig. 1. The XRD pattern for the starting material synthesized in this study for the solubility experiments on $Pr_2(C_2O_4)_3{\cdot}10H_2O$. The standard XRD patterns for $Pr_2(C_2O_4)_3{\cdot}10H_2O$ are included at the bottom part of the figure as the reference.

filled, the lids of the bottles were sealed with parafilm.

The supporting electrolytes are a series of HNO_3 solutions including 0.10 $mol{\cdot}kg^{-1}$, 0.50 and 1.0 $mol{\cdot}kg^{-1}$ HNO_3, and a series of mixtures of HNO_3 and $H_2C_2O_4$ (oxalic acid) including 1.94 $mol{\cdot}kg^{-1}$ HNO_3 + 0.017 $mol{\cdot}kg^{-1}$ $H_2C_2O_4$, 2.72 $mol{\cdot}kg^{-1}$ HNO_3 + 0.033 $mol{\cdot}kg^{-1}$ $H_2C_2O_4$, and 3.22 $mol{\cdot}kg^{-1}$ HNO_3 + 0.057 $mol{\cdot}kg^{-1}$ $H_2C_2O_4$. The supporting electrolyte solutions were prepared from degassed deionized (DI) water. The undersaturation solubility experiments were conducted at laboratory room temperature (23.0 ± 0.2 °C).

Solution samples were periodically withdrawn from experimental runs. Usually 3 mL solution was withdrawn from an experiment for each sampling. After a solution sample was withdrawn from an experiment and filtered with a 0.2 μm syringe filter using a BD® 3 mL syringe from Becton, Dickinson and Company. The Millex® 0.2 μm nylon syringe filter with a diameter of 25 mm is from MilliporeSigma®. The filtered solution was then weighed, acidified with 0.5 mL of concentrated TraceMetal® grade HNO_3 from Fisher Scientific, and finally diluted to a volume of 10 mL with DI water. If subsequent dilutions were needed, aliquots were taken from the first dilution samples for the second dilution, and aliquots of the second dilution were then taken for further dilution.

Praseodymium (Pr) and neodymium (Nd) concentrations of solutions were analyzed with a Perkin Elmer dual-view inductively coupled plasma-atomic emission spectrometer (ICP-AES) (Perkin Elmer DV 8300). Calibration blanks and standards were precisely matched with experimental matrices. The instrument was warmed-up for at least one and half hours before the calibration and analysis were performed. The instrument was calibrated with at least five standards (e.g., blank, 0.1 ppm Pr, 1.0 ppm Pr, 10 ppm Pr, 100 ppm Pr) with 1 ppm Sc as the internal standard. Immediately after the calibration, samples were analyzed. In the analysis, the calibration standards were also analyzed as samples to check if there were significant shifts. At least one calibration

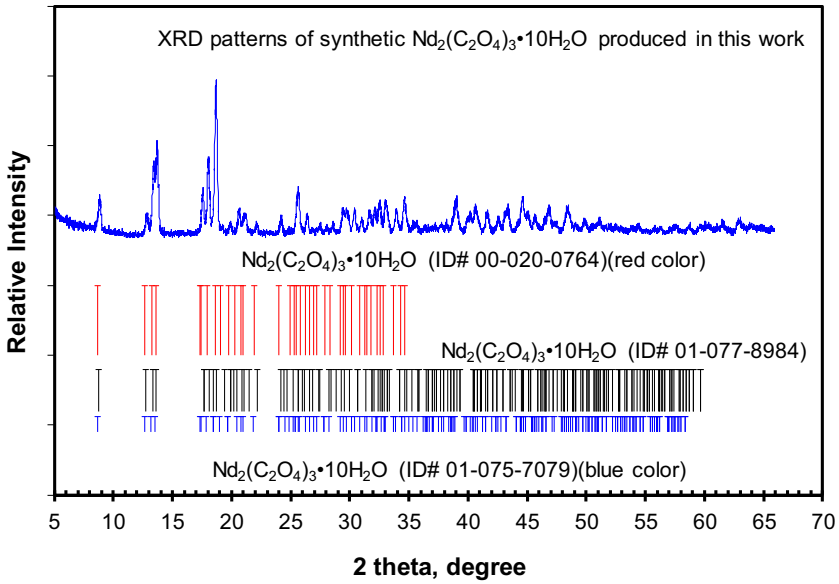


Fig. 2. The XRD pattern for the starting material synthesized in this study for the solubility experiments on $Nd_2(C_2O_4)_3{\cdot}10H_2O$. The standard XRD patterns for $Nd_2(C_2O_4)_3{\cdot}10H_2O$ are included at the bottom part of the figure as the reference.

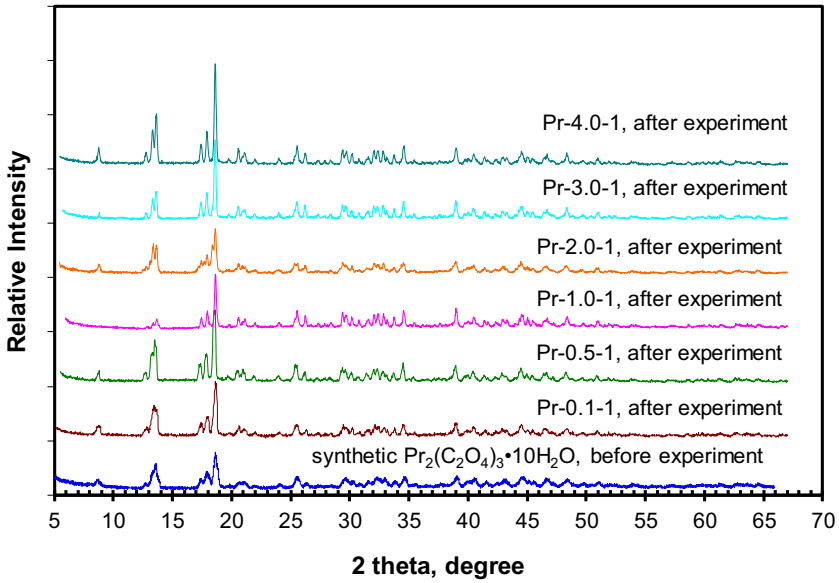


Fig. 3. The XRD patterns for the solid run products after experiment, from the solubility experiments on $Pr_2(C_2O_4)_3{\cdot}10H_2O$ in HNO_3 and the mixtures of HNO_3 and $H_2C_2O_4$. For the specific supporting medium, please refer to Table 1 for details.

standard and one blank were analyzed as samples after usually every eight samples were analyzed. If significant drifts (e.g., higher than 5%) from the known concentrations of the standards were observed, the instrument was re-calibrated. The detection limits (DL) for Pr and Nd are ~0.01 ppm. The lowest concentrations of Pr and Nd in our samples are at least ~1000 times higher than the DL. The linear correlation coefficients of calibration curves in all measurements were better than 0.9995. The analytical precision for ICP-AES is better than 1.00% in terms of the relative standard deviation (RSD) based on replicate analyses. Stoichiometric dissolution of praseodymium oxalate decahydrate and neodymium oxalate decahydrate was confirmed by analyzing for oxalate concentrations with a DIONEX ion chromatograph (IC) (DIONEX IC 1100) for selected samples. Solid phases were analyzed using a Bruker AXS D2 Phaser X-ray diffractometer, before and after experiments. All XRD patterns were collected using CuKα radiation at a scanning rate of 0.01765°/s for a 2θ range up to ~65°. The alignment of the XRD was checked by running a corundum standard.

3. Experimental results

3.1. Solid characterization

Shown in Fig. 1 is the XRD pattern of $Pr_2(C_2O_4)_3{\cdot}10H_2O$ synthesized in this study as the starting material for the solubility measurements. The standards for $Pr_2(C_2O_4)_3{\cdot}10H_2O$ from the PDF+4 database are included at the bottom part of Fig. 1. Fig. 1 demonstrates that $Pr_2(C_2O_4)_3{\cdot}10H_2O$ synthesized in this study is in excellent agreement with the standard $Pr_2(C_2O_4)_3{\cdot}10H_2O$. Similarly, the XRD pattern of $Nd_2(C_2O_4)_3{\cdot}10H_2O$ synthesized in this study as the starting material intended for the solubility measurements is shown in Fig. 2. Fig. 2 also demonstrates that $Nd_2(C_2O_4)_3{\cdot}10H_2O$ synthesized in this study is in excellent agreement with the standard $Nd_2(C_2O_4)_3{\cdot}10H_2O$ included at

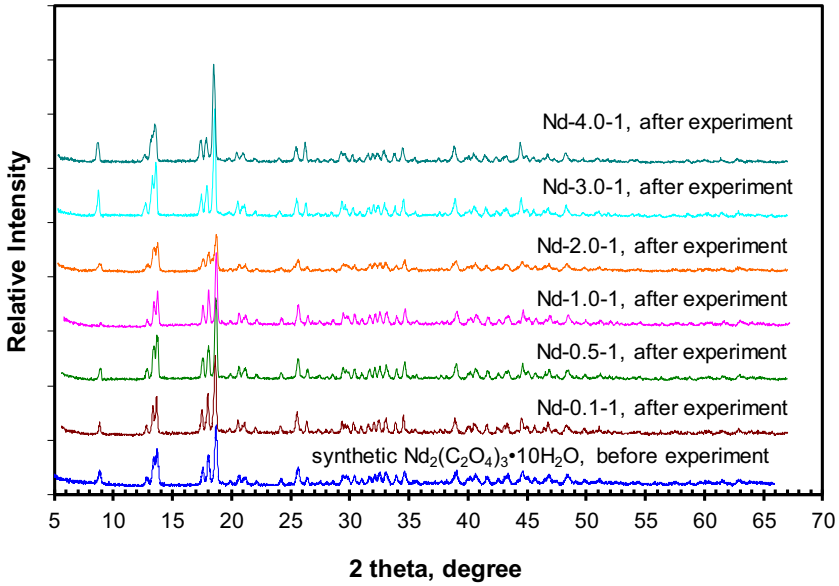


Fig. 4. The XRD patterns for the solid run products after experiment, from the solubility experiments on $Nd_2(C_2O_4)_3{\cdot}10H_2O$ in HNO_3 and the mixtures of HNO_3 and $H_2C_2O_4$. For the specific supporting medium, please refer to Table 2 for details.

Table 1
Experimental results of $Pr_2(C_2O_4)_3{\cdot}10H_2O$(cr) solubility in HNO_3 and mixtures of HNO_3 and $H_2C_2O_4$ at 23.0 ± 0.2 °C.

Experimental number	Supporting medium, mol·kg^{-1}	Experimental duration, days	Total praseodymium concentrations, mol·kg^{-1}, $m_{\Sigma Pr(III)}$
Pr-0.1-1	0.10, HNO_3	5	3.07E-04
Pr-0.5-1	0.50, HNO_3	5	2.32E-03
Pr-1.0-1	1.0, HNO_3	5	–
Pr-2.0-1	1.94, HNO_3, 0.017 $H_2C_2O_4$	5	1.32E-02
Pr-3.0-1	2.72, HNO_3, 0.033 $H_2C_2O_4$	5	1.88E-02
Pr-4.0-1	3.22, HNO_3, 0.057 $H_2C_2O_4$	5	2.11E-02
Pr-0.1-1	0.10, HNO_3	9	2.75E-04
Pr-0.5-1	0.50, HNO_3	9	2.28E-03
Pr-1.0-1	1.0, HNO_3	9	–
Pr-2.0-1	1.94, HNO_3, 0.017 $H_2C_2O_4$	9	1.17E-02
Pr-3.0-1	2.72, HNO_3, 0.033 $H_2C_2O_4$	9	1.90E-02
Pr-4.0-1	3.22, HNO_3, 0.057 $H_2C_2O_4$	9	2.05E-02
Pr-0.1-1	0.10, HNO_3	15	3.14E-04
Pr-0.5-1	0.50, HNO_3	15	2.37E-03
Pr-1.0-1	1.0, HNO_3	15	–
Pr-2.0-1	1.94, HNO_3, 0.017 $H_2C_2O_4$	15	1.20E-02
Pr-3.0-1	2.72, HNO_3, 0.033 $H_2C_2O_4$	15	1.91E-02
Pr-4.0-1	3.22, HNO_3, 0.057 $H_2C_2O_4$	15	2.09E-02
Pr-0.1-1	0.10, HNO_3	26	2.70E-04
Pr-0.5-1	0.50, HNO_3	26	2.17E-03
Pr-1.0-1	1.0, HNO_3	26	–
Pr-2.0-1	1.94, HNO_3, 0.017 $H_2C_2O_4$	26	–
Pr-3.0-1	2.72, HNO_3, 0.033 $H_2C_2O_4$	26	1.75E-02
Pr-4.0-1	3.22, HNO_3, 0.057 $H_2C_2O_4$	26	1.97E-02
Pr-0.1-1	0.10, HNO_3	33	2.78E-04
Pr-0.5-1	0.50, HNO_3	33	2.15E-03
Pr-1.0-1	1.0, HNO_3	33	6.28E-03
Pr-2.0-1	1.94, HNO_3, 0.017 $H_2C_2O_4$	33	1.15E-02
Pr-3.0-1	2.72, HNO_3, 0.033 $H_2C_2O_4$	33	1.76E-02
Pr-4.0-1	3.22, HNO_3, 0.057 $H_2C_2O_4$	33	1.93E-02
Pr-0.1-1	0.10, HNO_3	36	2.66E-04
Pr-0.5-1	0.50, HNO_3	36	2.10E-03
Pr-1.0-1	1.0, HNO_3	36	6.28E-03
Pr-2.0-1	1.94, HNO_3, 0.017 $H_2C_2O_4$	36	1.12E-02
Pr-3.0-1	2.72, HNO_3, 0.033 $H_2C_2O_4$	36	–
Pr-4.0-1	3.22, HNO_3, 0.057 $H_2C_2O_4$	36	–
Pr-0.1-1	0.10, HNO_3	126	3.20E-04
Pr-0.5-1	0.50, HNO_3	126	2.38E-03
Pr-1.0-1	1.0, HNO_3	126	6.14E-03
Pr-2.0-1	1.94, HNO_3, 0.017 $H_2C_2O_4$	126	1.10E-02
Pr-3.0-1	2.72, HNO_3, 0.033 $H_2C_2O_4$	126	1.66E-02
Pr-4.0-1	3.22, HNO_3, 0.057 $H_2C_2O_4$	126	1.86E-02
Pr-0.1-1	0.10, HNO_3	135	3.08E-04
Pr-0.5-1	0.50, HNO_3	135	2.38E-03
Pr-1.0-1	1.0, HNO_3	135	6.01E-03
Pr-2.0-1	1.94, HNO_3, 0.017 $H_2C_2O_4$	135	1.04E-02
Pr-3.0-1	2.72, HNO_3, 0.033 $H_2C_2O_4$	135	1.64E-02
Pr-4.0-1	3.22, HNO_3, 0.057 $H_2C_2O_4$	135	1.83E-02
Pr-0.1-1	0.10, HNO_3	147	3.20E-04
Pr-0.5-1	0.50, HNO_3	147	2.41E-03
Pr-1.0-1	1.0, HNO_3	147	6.01E-03
Pr-2.0-1	1.94, HNO_3, 0.017 $H_2C_2O_4$	147	1.10E-02
Pr-3.0-1	2.72, HNO_3, 0.033 $H_2C_2O_4$	147	1.86E-02
Pr-4.0-1	3.22, HNO_3, 0.057 $H_2C_2O_4$	147	1.86E-02
Pr-0.1-1	0.10, HNO_3	152	3.14E-04
Pr-0.5-1	0.50, HNO_3	152	2.40E-03
Pr-1.0-1	1.0, HNO_3	152	6.03E-03
Pr-2.0-1	1.94, HNO_3, 0.017 $H_2C_2O_4$	152	1.07E-02
Pr-3.0-1	2.72, HNO_3, 0.033 $H_2C_2O_4$	152	1.64E-02
Pr-4.0-1	3.22, HNO_3, 0.057 $H_2C_2O_4$	152	1.80E-02

the bottom part of Fig. 2. The detailed comparisons, in terms of d-spacing, of the major peaks of $Pr_2(C_2O_4)_3{\cdot}10H_2O$ and $Nd_2(C_2O_4)_3{\cdot}10H_2O$ with the respective standards are tabulated in Appendices A and B, which again show that the synthetic phases are in excellent agreement with the standards.

In Fig. 3, the XRD patterns for the starting material (i.e., before experiment) and the run products (i.e., after experiment) for the solubility experiments on $Pr_2(C_2O_4)_3{\cdot}10H_2O$ are presented. The XRD patterns in Fig. 3 clearly indicate that there is no phase change, and $Pr_2(C_2O_4)_3{\cdot}10H_2O$ is the solubility-controlling phase in each experiment from Pr-0.1-1 through Pr-4.0-1.

Similarly, the XRD patterns for the solubility experiments on $Nd_2(C_2O_4)_3{\cdot}10H_2O$ are displayed in Fig. 4. The XRD patterns in Fig. 4 also clearly demonstrate that there is no phase change for all of experiments, and $Nd_2(C_2O_4)_3{\cdot}10H_2O$ is the solubility-controlling phase in every experiment from Nd-0.1-1 through Nd-4.0-1.

3.2. Solution chemistry data

In Table 1, total Pr(III) concentrations in equilibrium with $Pr_2(C_2O_4)_3{\cdot}10H_2O$ on a molal scale are presented. Fig. 5 displays total Pr (III) concentrations as a function of experimental duration. The concentration data displayed in Fig. 5 suggest that the equilibrium was attained in the first sampling. The figure also shows that Pr(III) concentrations in the experiments having HNO_3 only increase with concentration of HNO_3. In the experiments with the mixtures of HNO_3 and $H_2C_2O_4$, the presence of $H_2C_2O_4$ suppresses the solubility of $Pr_2(C_2O_4)_3{\cdot}10H_2O$.

In Table 2, total Nd(III) concentrations in equilibrium with $Nd_2(C_2O_4)_3{\cdot}10H_2O$ on a molal scale are presented. In comparison with the results for the experiments with $Pr_2(C_2O_4)_3{\cdot}10H_2O$ (Table 1), the solubilities of $Nd_2(C_2O_4)_3{\cdot}10H_2O$ are slightly, systematically, lower. The solubilities of $Pr_2(C_2O_4)_3{\cdot}10H_2O$ are systematically ~1.3 times of those of $Nd_2(C_2O_4)_3{\cdot}10H_2O$. Fig. 6 displays total Nd(III) concentrations as a function of experimental duration. The data indicate that the equilibrium was attained in the first sampling, as for the experiments with $Pr_2(C_2O_4)_3{\cdot}10H_2O$. The figure also indicates that Nd(III) concentrations in the experiments having HNO_3 only increase with concentration of HNO_3. In the experiments with the mixtures of HNO_3 and $H_2C_2O_4$, the presence of $H_2C_2O_4$ reduces the solubility of $Nd_2(C_2O_4)_3{\cdot}10H_2O$, as observed in the experiments with $Pr_2(C_2O_4)_3{\cdot}10H_2O$.

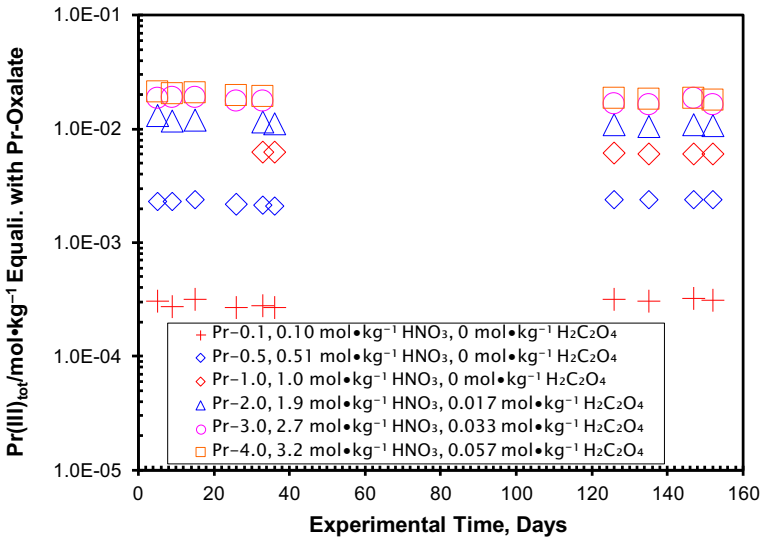


Fig. 5. A plot showing total praseodymium concentrations on a molal scale ($m_{\Sigma Pr(III)}$) as a function of experimental duration from the solubility measurements on $Pr_2(C_2O_4)_3{\cdot}10H_2O$ in HNO_3 and the mixtures of HNO_3 and $H_2C_2O_4$.

4. Thermodynamic calculations and model

4.1. Method for thermodynamic modeling

In this study, the standard state for a solid phase is defined as its pure end-member with unit activity at temperatures and pressures of interest. The standard state of the solvent in aqueous solutions is pure solvent at temperatures and pressures of interest. The standard state for an aqueous solute is a hypothetical 1 molal ($mol{\cdot}kg^{-1}$) solution of infinite dilution at temperatures and pressures of interest.

Thakur et al. (2015) established a Pitzer model for describing dissociation constants of oxalic acid and stability constants for actinide oxalate complexes such as $AmC_2O_4^+$ (β_{101}) and $Am(C_2O_4)_2^-$ (β_{102}) to high ionic strengths up to 6.6 $mol{\cdot}kg^{-1}$. The stability constants of $AmC_2O_4^+$ and $Am(C_2O_4)_2^-$ obtained by Thakur et al. (2015) are in excellent agreement with those of Brunel et al. (2015), who determined them by using the capillary electrophoresis coupled with inductively coupled plasma mass spectrometry (CE-ICP-MS).

In this study, we adopt the model of Thakur et al. (2015) for the oxalate system as the basis to evaluate solubility data of $Pr_2(C_2O_4)_3{\cdot}10H_2O$, and $Nd_2(C_2O_4)_3{\cdot}10H_2O$ in mixtures of HNO_3 and $H_2C_2O_4$. We evaluate the parameters including the stability constants and Pitzer parameters for Ln(III) for all of these two phases.

The computer code EQ3/6 Version 8.0a (Wolery et al., 2010; Xiong, 2011a) with actinide chemistry from (Xiong, 2011b) is employed as the modeling platform, and the parameters for the oxalate species are listed in Tables 3 and 4. The goal of the modeling is to minimize the difference between experimental and model predicted values. A similar modeling approach can be found in some of the previous work (e.g., Xiong, 2015, 2018; Xiong et al., 2017a, 2017b). (See Table 5.)

In the modeling, experimental data are used to generate EQ3/6 input files in the first step. In the second step, the values of the targeted parameter (e.g., log *K*) are adjusted until the difference between experimental values (e.g., $m_{\Sigma Pr(III)}$, $m_{\Sigma Nd(III)}$) and model-produced values predicted by the computer code is minimized. In the third step, the final selected value for the targeted parameter is verified to see how it reproduces experimental data.

The uncertainties reported in this study are two standard deviations (2σ), including those accounted for the small deviation of the experimental temperature from the standard temperature of 25 °C. Error propagations are calculated based on uncertainties associated with regressions and equilibrium constants in the model.

In this work, the raw solubility data of $Pr_2(C_2O_4)_3{\cdot}10H_2O$ and $Nd_2(C_2O_4)_3{\cdot}10H_2O$ at 23.0 ± 0.2 °C, in mixtures of HNO_3 and $H_2C_2O_4$ obtained in this study are used for modeling the equilibrium constants for the following reactions,

$$Pr_2(C_2O_4)_3{\cdot}10H_2O \rightleftharpoons 2Pr^{3+} + 3C_2O_4^{2-} + 10H_2O(l) \quad (1)$$

$$Nd_2(C_2O_4)_3{\cdot}10H_2O \rightleftharpoons 2Nd^{3+} + 3C_2O_4^{2-} + 10H_2O(l) \quad (2)$$

4.2. Results of thermodynamic modeling

In Table 3, the solubility product constants at infinite dilution for $Pr_2(C_2O_4)_3{\cdot}10H_2O$, $Nd_2(C_2O_4)_3{\cdot}10H_2O$, $Pu_2(C_2O_4)_3{\cdot}10H_2O$, $Am_2(C_2O_4)_3{\cdot}10H_2O$, and $Cm_2(C_2O_4)_3{\cdot}10H_2O$ at 25 °C, consistent with the Thakur et al. (2015) oxalate system, are tabulated. Among them, the solubility product constant for $Pu_2(C_2O_4)_3{\cdot}10H_2O$ for Reaction (3) is based on the analog of $Pr_2(C_2O_4)_3{\cdot}10H_2O$, and those for $Am_2(C_2O_4)_3{\cdot}10H_2O$ and $Cm_2(C_2O_4)_3{\cdot}10H_2O$ for Reactions (4) and (5) are in accordance with the analog of $Nd_2(C_2O_4)_3{\cdot}10H_2O$,

$$Pu_2(C_2O_4)_3{\cdot}10H_2O \rightleftharpoons 2Pu^{3+} + 3C_2O_4^{2-} + 10H_2O(l) \quad (3)$$

$$Am_2(C_2O_4)_3{\cdot}10H_2O \rightleftharpoons 2Am^{3+} + 3C_2O_4^{2-} + 10H_2O(l) \quad (4)$$

$$Cm_2(C_2O_4)_3{\cdot}10H_2O \rightleftharpoons 2Cm^{3+} + 3C_2O_4^{2-} + 10H_2O(l) \quad (5)$$

The Pitzer binary interaction parameters for $Pr^{3+}/Nd^{3+}/Pu^{3+}/Am^{3+}/Cm^{3+}$—$NO_3^-$ and the mixing parameter (θ) for $Pr^{3+}/Nd^{3+}/Pu^{3+}/Am^{3+}/Cm^{3+}$—$H^+$ evaluated in this study, along with the auxiliary parameters from Thakur et al. (2015), are listed in Table 4.

In a previous study, the solubility product constants for REE(III)-oxalates were evaluated by using the Specific Ion Interaction Theory (SIT) (Xiong, 2011c), which range from −29.15 ± 0.35 for La(III)-oxalate to −32.31 ± 0.50 for Gd(III)-oxalate (Xiong, 2011c). The solubility product constants for Pr(III)- and Nd(III)-oxalate decahydrates obtained in this study are highly consistent with the values for the corresponding Pr(III) and Nd(III) anhydrous oxalates determined before (−30.91 ± 0.42 for Pr(III)-oxalate and −31.57 ± 0.62) (Xiong, 2011c) (Table 3).

In Fig. 7, experimental solubilities of $Pr_2(C_2O_4)_3{\cdot}10H_2O$ and $Pu_2(C_2O_4)_3{\cdot}10H_2O$ expressed as total molalities of Pr(III), $m_{\Sigma Pr(III)}$, and Pu(III), $m_{\Sigma Pu(III)}$, as a function of molalities of HNO_3 at constant molalities of $H_2C_2O_4$ ranging from 0.0 through 0.1 $mol{\cdot}kg^{-1}$, are compared with those predicted by the model developed by this study. All of the

Table 2
Experimental results of $Nd_2(C_2O_4)_3{\cdot}10H_2O$(cr) solubility in HNO_3 and mixtures of HNO_3 and $H_2C_2O_4$ at 23.0 ± 0.2 °C.

Experimental number	Supporting medium, mol·kg^{-1}	Experimental duration, days	Total neodymium concentrations, mol·kg^{-1}, $m_{\Sigma Nd(III)}$
Nd-0.1-1	0.10, HNO_3	5	2.37E-04
Nd-0.5-1	0.50, HNO_3	5	1.99E-03
Nd-1.0-1	1.0, HNO_3	5	–
Nd-2.0-1	1.94, HNO_3, 0.017 $H_2C_2O_4$	5	9.46E-03
Nd-3.0-1	2.72, HNO_3, 0.033 $H_2C_2O_4$	5	1.37E-02
Nd-4.0-1	3.22, HNO_3, 0.057 $H_2C_2O_4$	5	1.39E-02
Nd-0.1-1	0.10, HNO_3	8	2.46E-04
Nd-0.5-1	0.50, HNO_3	8	2.03E-03
Nd-1.0-1	1.0, HNO_3	8	–
Nd-2.0-1	1.94, HNO_3, 0.017 $H_2C_2O_4$	8	–
Nd-3.0-1	2.72, HNO_3, 0.033 $H_2C_2O_4$	8	1.33E-02
Nd-4.0-1	3.22, HNO_3, 0.057 $H_2C_2O_4$	8	1.26E-02
Nd-0.1-1	0.10, HNO_3	14	2.47E-04
Nd-0.5-1	0.50, HNO_3	14	2.10E-03
Nd-1.0-1	1.0, HNO_3	14	–
Nd-2.0-1	1.94, HNO_3, 0.017 $H_2C_2O_4$	14	9.12E-03
Nd-3.0-1	2.72, HNO_3, 0.033 $H_2C_2O_4$	14	1.33E-02
Nd-4.0-1	3.22, HNO_3, 0.057 $H_2C_2O_4$	14	1.44E-02
Nd-0.1-1	0.10, HNO_3	25	2.50E-04
Nd-0.5-1	0.50, HNO_3	25	2.08E-03
Nd-1.0-1	1.0, HNO_3	25	5.30E-03
Nd-2.0-1	1.94, HNO_3, 0.017 $H_2C_2O_4$	25	8.15E-03
Nd-3.0-1	2.72, HNO_3, 0.033 $H_2C_2O_4$	25	1.22E-02
Nd-4.0-1	3.22, HNO_3, 0.057 $H_2C_2O_4$	25	1.23E-02
Nd-0.1-1	0.10, HNO_3	32	2.50E-04
Nd-0.5-1	0.50, HNO_3	32	2.05E-03
Nd-1.0-1	1.0, HNO_3	32	5.35E-03
Nd-2.0-1	1.94, HNO_3, 0.017 $H_2C_2O_4$	32	8.35E-03
Nd-3.0-1	2.72, HNO_3, 0.033 $H_2C_2O_4$	32	1.28E-02
Nd-4.0-1	3.22, HNO_3, 0.057 $H_2C_2O_4$	32	1.25E-02
Nd-0.1-1	0.10, HNO_3	35	2.45E-04
Nd-0.5-1	0.50, HNO_3	35	2.03E-03
Nd-1.0-1	1.0, HNO_3	35	5.27E-03
Nd-2.0-1	1.94, HNO_3, 0.017 $H_2C_2O_4$	35	8.34E-03
Nd-3.0-1	2.72, HNO_3, 0.033 $H_2C_2O_4$	35	1.23E-02
Nd-4.0-1	3.22, HNO_3, 0.057 $H_2C_2O_4$	35	1.28E-02
Nd-0.1-1	0.10, HNO_3	125	2.51E-04
Nd-0.5-1	0.50, HNO_3	125	2.06E-03
Nd-1.0-1	1.0, HNO_3	125	5.03E-03
Nd-2.0-1	1.94, HNO_3, 0.017 $H_2C_2O_4$	125	7.83E-03
Nd-3.0-1	2.72, HNO_3, 0.033 $H_2C_2O_4$	125	1.30E-02
Nd-4.0-1	3.22, HNO_3, 0.057 $H_2C_2O_4$	125	1.33E-02
Nd-0.1-1	0.10, HNO_3	134	2.50E-04
Nd-0.5-1	0.50, HNO_3	134	2.06E-03
Nd-1.0-1	1.0, HNO_3	134	4.99E-03
Nd-2.0-1	1.94, HNO_3, 0.017 $H_2C_2O_4$	134	7.31E-03
Nd-3.0-1	2.72, HNO_3, 0.033 $H_2C_2O_4$	134	1.30E-02
Nd-4.0-1	3.22, HNO_3, 0.057 $H_2C_2O_4$	134	–
Nd-0.1-1	0.10, HNO_3	148	2.51E-04
Nd-0.5-1	0.50, HNO_3	148	2.02E-03
Nd-1.0-1	1.0, HNO_3	148	5.00E-03
Nd-2.0-1	1.94, HNO_3, 0.017 $H_2C_2O_4$	148	8.02E-03
Nd-3.0-1	2.72, HNO_3, 0.033 $H_2C_2O_4$	148	1.34E-02
Nd-4.0-1	3.22, HNO_3, 0.057 $H_2C_2O_4$	148	1.34E-02
Nd-0.1-1	0.10, HNO_3	151	2.65E-04
Nd-0.5-1	0.50, HNO_3	151	2.01E-03
Nd-1.0-1	1.0, HNO_3	151	5.02E-03
Nd-2.0-1	1.94, HNO_3, 0.017 $H_2C_2O_4$	151	7.73E-03
Nd-3.0-1	2.72, HNO_3, 0.033 $H_2C_2O_4$	151	1.31E-02
Nd-4.0-1	3.22, HNO_3, 0.057 $H_2C_2O_4$	151	1.37E-02

experimental data on $Pu_2(C_2O_4)_3{\cdot}10H_2O$ are not used in the model development. The solubility data for $Pu_2(C_2O_4)_3{\cdot}10H_2O$ from the literature include Porter and Symonds Jr (1965), Burney and Porter (1967), Cheneau (1971), Sun et al. (1987), and Hasilkar et al. (1994). Fig. 7 indicates that the values predicted by our model are in excellent agreement with the experimental data on $Pu_2(C_2O_4)_3{\cdot}10H_2O$.

Fig. 8 shows the comparisons of the model-predicted values with the experimental data from the literature at a constant molality of $H_2C_2O_4$ at 0.2 mol·kg^{-1}. It should be noted again that the solubility data for $Pu_2(C_2O_4)_3{\cdot}10H_2O$ from the literature are not used in the model development. The model-predicted values at 0.0 mol·kg^{-1} $H_2C_2O_4$ are also included as a reference to illustrate how the change in $H_2C_2O_4$ concentration affects the solubility of $Pr_2(C_2O_4)_3{\cdot}10H_2O$ or $Pu_2(C_2O_4)_3{\cdot}10H_2O$. The literature sources for the solubility data for $Pu_2(C_2O_4)_3{\cdot}10H_2O$ are the same as those in Fig. 7, with the addition of Doty and Chong (1970). Again, the values predicted by our model are in good agreement with the experimental data for $Pu_2(C_2O_4)_3{\cdot}10H_2O$.

Fig. 9 displays the Pr(III)/Pu(III) concentrations in equilibrium with $Pr_2(C_2O_4)_3{\cdot}10H_2O$/$Pu_2(C_2O_4)_3{\cdot}10H_2O$ predicted by our model, in comparison with the experimental data for $Pu_2(C_2O_4)_3{\cdot}10H_2O$ from the literature at a constant molality of $H_2C_2O_4$ at 0.3 mol·kg^{-1}. Again the solubility data for $Pu_2(C_2O_4)_3{\cdot}10H_2O$ from the literature are independent of the model development. The model-predicted values at 0.0 mol·kg^{-1} $H_2C_2O_4$ are also included as a reference to illustrate how the change in $H_2C_2O_4$ concentration affects the solubility of $Pr_2(C_2O_4)_3{\cdot}10H_2O$ or $Pu_2(C_2O_4)_3{\cdot}10H_2O$, as done in Figs. 7 and 8. Fig. 9 shows that the solubilities predicted by our model are in good agreement with the experimental data for $Pu_2(C_2O_4)_3{\cdot}10H_2O$. Of note, the experimental data from Sun et al. (1987) below 1.0 mol·kg^{-1} HNO_3 deviate from those from other researchers (i.e., Porter and Symonds Jr, 1965; Burney and Porter, 1967; Cheneau, 1971) and from the model. This also occurs at other concentrations of $H_2C_2O_4$ (see Figs. 7 and 8). This may be due to the systematic experimental errors in the low ionic strength range in Sun et al. (1987).

In summary, as illustrated by Figs. 7 through 9, the good agreement between the values predicted by our model and the experimental data on $Pu_2(C_2O_4)_3{\cdot}10H_2O$ from the literature not only validates our model but also demonstrates that Pr(III) is an excellent analog to Pu(III).

Figs. 10 through 12 show the comparisons of Am(III)/Cm(III) concentrations in equilibrium with $Am_2(C_2O_4)_3{\cdot}10H_2O$/$Cm_2(C_2O_4)_3{\cdot}10H_2O$ as a function of HNO_3 concentrations at the constant background $H_2C_2O_4$ concentrations ranging from 0 to 0.25 mol·kg^{-1} predicted by our model with the experimental data from the literature. All of the

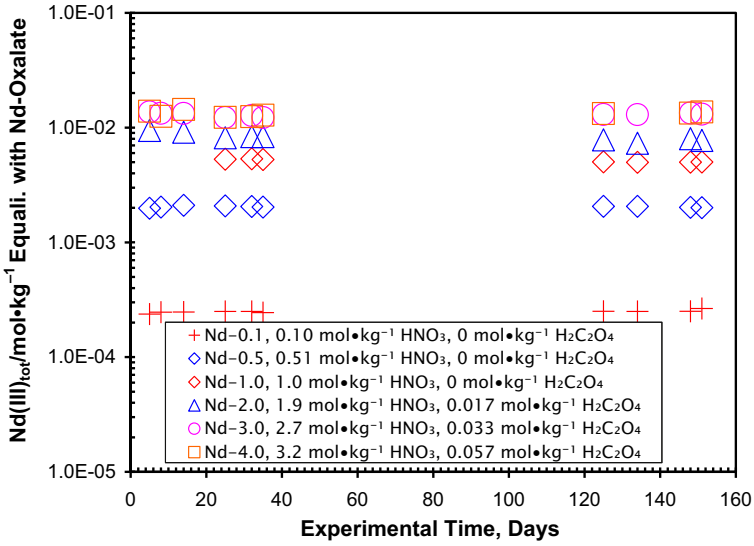


Fig. 6. A plot showing total neodymium concentrations on a molal scale ($m_{\Sigma Nd(III)}$) as a function of experimental duration from the solubility measurements on $Nd_2(C_2O_4)_3{\cdot}10H_2O$ in HNO_3 and the mixtures of HNO_3 and $H_2C_2O_4$.

Table 3
Thermodynamic model for dissociation of oxalic acid and stabilities of $AmC_2O_4^+$ and $Am(C_2O_4)_2^-$ adopted by this work, and equilibrium constants for Pu(III), Am(III), and Cm(III) oxalates at infinite dilution, 25 °C and 1 bar evaluated by this study.

Reactions	log K or log β_n	Reference and remarks
$H_2C_2O_4 \rightleftharpoons H^+ + HC_2O_4^-$	-1.71 ± 0.15	Thakur et al. (2015)
$HC_2O_4^- \rightleftharpoons H^+ + C_2O_4^{2-}$	-4.36 ± 0.15	Thakur et al. (2015)
$Am^{3+} + C_2O_4^{2-} \rightleftharpoons AmC_2O_4^+$	6.30 ± 0.06	Thakur et al. (2015)
$Am^{3+} + 2C_2O_4^{2-} \rightleftharpoons Am(C_2O_4)_2^-$	10.84 ± 0.06	Thakur et al. (2015)
$Pr_2(C_2O_4)_3{\cdot}10H_2O \rightleftharpoons 2Pr^{3+} + 3C_2O_4^{2-} + 10H_2O(l)$	-30.82 ± 0.30	This study, based on $Pr_2(C_2O_4)_3{\cdot}10H_2O$ solubility data in $HNO_3 + H_2C_2O_4$
$Nd_2(C_2O_4)_3{\cdot}10H_2O \rightleftharpoons 2Nd^{3+} + 3C_2O_4^{2-} + 10H_2O(l)$	-31.14 ± 0.35	This study, based on $Nd_2(C_2O_4)_3{\cdot}10H_2O$ solubility data in $HNO_3 + H_2C_2O_4$
$Pu_2(C_2O_4)_3{\cdot}10H_2O \rightleftharpoons 2Pu^{3+} + 3C_2O_4^{2-} + 10H_2O(l)$	-30.82 ± 0.30	This study, based on the analog of $Pr_2(C_2O_4)_3{\cdot}10H_2O$ to $Pu_2(C_2O_4)_3{\cdot}10H_2O$
$Am_2(C_2O_4)_3{\cdot}10H_2O \rightleftharpoons 2Am^{3+} + 3C_2O_4^{2-} + 10H_2O(l)$	-31.14 ± 0.35	This study, based on the analog of $Nd_2(C_2O_4)_3{\cdot}10H_2O$ to $Am_2(C_2O_4)_3{\cdot}10H_2O$
$Cm_2(C_2O_4)_3{\cdot}10H_2O \rightleftharpoons 2Cm^{3+} + 3C_2O_4^{2-} + 10H_2O(l)$	-31.14 ± 0.35	This study, based on the analog of $Nd_2(C_2O_4)_3{\cdot}10H_2O$ to $Cm_2(C_2O_4)_3{\cdot}10H_2O$

experimental data from the literature are not used in our model development. The model-predicted values at 0.0 mol·kg^{-1} $H_2C_2O_4$ are included in these three figures as a reference to illustrate how the change in $H_2C_2O_4$ concentration affects the solubility of $Am_2(C_2O_4)_3{\cdot}10H_2O$ or $Cm_2(C_2O_4)_3{\cdot}10H_2O$.

The results at 0.025 to 0.05 mol·kg^{-1} $H_2C_2O_4$ are displayed in Fig. 10. The sources for the experimental data include Burney and Porter (1967) for both $Am_2(C_2O_4)_3{\cdot}10H_2O$ and $Cm_2(C_2O_4)_3{\cdot}10H_2O$, and Zakolupin and Korablin (1977) for $Am_2(C_2O_4)_3{\cdot}10H_2O$. The values predicted by our model are in good agreement with the experimental data.

Fig. 11 depicts the results at a constant background $H_2C_2O_4$ concentration of 0.1 mol·kg^{-1}. The sources for the experimental data for $Am_2(C_2O_4)_3{\cdot}10H_2O$ and $Cm_2(C_2O_4)_3{\cdot}10H_2O$ are the same as those in Fig. 10, with the addition of Campbell et al. (2016) for $Am_2(C_2O_4)_3{\cdot}10H_2O$. Fig. 11 indicates that the model-predicted values are in excellent agreement with the experimental data.

Fig. 12 presents the results at a constant background $H_2C_2O_4$ concentration of 0.25 mol·kg^{-1}. The sources for the experimental data for $Am_2(C_2O_4)_3{\cdot}10H_2O$ and $Cm_2(C_2O_4)_3{\cdot}10H_2O$ are the same as those in Fig. 10. Fig. 12 indicates that the model-predicted values are in close agreement with the experimental data.

In summary, as shown by Figs. 10 through 12, our model for $Nd_2(C_2O_4)_3{\cdot}10H_2O$ predicts the Am(III) and Cm(III) concentrations in equilibrium with $Am_2(C_2O_4)_3{\cdot}10H_2O$ and $Cm_2(C_2O_4)_3{\cdot}10H_2O$ in agreement with those from the literature, validating our model as well as demonstrating that $Nd_2(C_2O_4)_3{\cdot}10H_2O$ is a good analog to $Am_2(C_2O_4)_3{\cdot}10H_2O$ and $Cm_2(C_2O_4)_3{\cdot}10H_2O$.

5. Applications

5.1. Interactions of oxalate with actinides under the surface and subsurface conditions in contaminated sites

There have been several sites on the Earth surface that have been contaminated by the radioactive materials including transuranic nuclides. The sites include the Chernobyl (e.g., Zhdanova et al., 2000), the Lake Karachai area (Solodov et al., 1994; Rumynin, 2011), and a number of sites in U.S.A. (Cantrell and Riley, 2008). Among those sites, the Chernobyl and Lake Karachai are of particular interest, because the presence of oxalate at these sites have been already reported or inferred. At the Chernobyl site, it has been observed that there are extensive fungal growths in the building structures (Zhdanova et al., 2000). Notice that the extensive fungal growths are remarkable, as it has been demonstrated that fungi can successfully colonize barrier concretes used for nuclear waste disposal, and produce oxalate during this process (Fomina et al., 2007; Gadd et al., 2014), resulting in the formation of whewellite ($CaC_2O_4{\cdot}H_2O$) and weddellite ($CaC_2O_4{\cdot}2H_2O$). Therefore, the observations of extensive fungal growths at the Chernobyl site indicate that fungi can be very radiation-resistant, and can survive and populate in radiation environments on one hand, and oxalate can be generated on the other hand. Consequently, the interactions of oxalate with actinides such as Am(III) released in the accident (e.g., Krivokhatsky et al., 1991) at the Chernobyl site are expected, as it has been observed that Pu and Am are dominantly organically bound in the soils at Chernobyl site (Lujaniene et al., 2002), and are worth further studying, especially in light of the recent finding of deveroite-(Ce) in

Table 4
Pitzer binary interaction and mixing parameters evaluated in this work.

Species *i*	Species *j*	$\beta^{(0)}$	$\beta^{(1)}$	C^{ϕ}	Reference
$(Pr/Nd/Pu/Am/Cm)^{3+}$	NO_3^-	0.7642	5.22[a]	0	This work
Na^+	$HC_2O_4^-$	−0.2886	0.29	0.068	Thakur et al. (2015)
Na^+	$C_2O_4^{2-}$	−0.2770	1.74	0.122	Thakur et al. (2015)
K^+	$HC_2O_4^-$	−0.2886	0.29	0.068	Using the values from Thakur et al. (2015) for Na^+ as analogs for interaction with K^+
K^+	$C_2O_4^{2-}$	−0.2770	1.74	0.122	Using the values from Thakur et al. (2015) for Na^+ as analogs for interaction with K^+
$AmC_2O_4^+$	Cl^-	−0.9374	0.29	0.248	Choppin et al. (2001)
$AmC_2O_4^+$	ClO_4^-	−0.7655	0.29	0.2424	Thakur et al. (2015)
Na^+	$Am(C_2O_4)_2^-$	−1.4349	0.29	0.3718	Thakur et al. (2015)
K^+	$Am(C_2O_4)_2^-$	−1.4349	0.29	0.3718	Using the values from Thakur et al. (2015) for Na^+ as analogs for interaction with K^+
Species *i*	Species *j*	Species *k*	θ_{ij}	ζ_{ijk}	
$(Pr/Nd/Pu/Am/Cm)^{3+}$	H^+		0.3051		This work
$(Pr/Nd/Pu/Am/Cm)^{3+}$	NO_3^-	$H_2C_2O_4(aq)$		0.2382	This work

[a] This parameter is not evaluated in this work. It is set to the average value for 3:1 and 1:3 interactions, according to the paradigm of Choppin et al. (2001).

Table 5
Comparison of solubility product constants of actinide oxalates at infinite dilution, 25 °C and 1 bar determined in this study, with those for lanthanide oxalates from Xiong (2011c).

Reactions	log K_{sp}	Remarks
$Pr_2(C_2O_4)_3{\cdot}10H_2O \rightleftharpoons 2Pr^{3+} + 3C_2O_4^{2-} + 10H_2O(l)$	−30.82 ± 0.30	This study, based on $Pr_2(C_2O_4)_3{\cdot}10H_2O$ solubility data in $HNO_3 + H_2C_2O_4$, Pitzer model
$Nd_2(C_2O_4)_3{\cdot}10H_2O \rightleftharpoons 2Nd^{3+} + 3C_2O_4^{2-} + 10H_2O(l)$	−31.14 ± 0.35	This study, based on $Nd_2(C_2O_4)_3{\cdot}10H_2O$ solubility data in $HNO_3 + H_2C_2O_4$, Pitzer model
$Pu_2(C_2O_4)_3{\cdot}10H_2O \rightleftharpoons 2Pu^{3+} + 3C_2O_4^{2-} + 10H_2O(l)$	−30.82 ± 0.30 (2σ)	This study, based on the analog of $Pr_2(C_2O_4)_3{\cdot}10H_2O$ to $Pu_2(C_2O_4)_3{\cdot}10H_2O$, Pitzer model
$Am_2(C_2O_4)_3{\cdot}10H_2O \rightleftharpoons 2Am^{3+} + 3C_2O_4^{2-} + 10H_2O(l)$	−31.14 ± 0.35 (2σ)	This study, based on the analog of $Nd_2(C_2O_4)_3{\cdot}10H_2O$ to $Am_2(C_2O_4)_3{\cdot}10H_2O$, Pitzer model
$Cm_2(C_2O_4)_3{\cdot}10H_2O \rightleftharpoons 2Cm^{3+} + 3C_2O_4^{2-} + 10H_2O(l)$	−31.14 ± 0.35 (2σ)	This study, based on the analog of $Nd_2(C_2O_4)_3{\cdot}10H_2O$ to $Cm_2(C_2O_4)_3{\cdot}10H_2O$, Pitzer model
$Pr_2(C_2O_4)_3 \rightleftharpoons 2Pr^{3+} + 3C_2O_4^{2-}$	−30.91 ± 0.42 (2σ)	Xiong (2011c), SIT model
$Nd_2(C_2O_4)_3 \rightleftharpoons 2Nd^{3+} + 3C_2O_4^{2-}$	−31.57 ± 0.62 (2σ)	Xiong (2011c), SIT model

nature (Guastoni et al., 2013) (see the following section for detail).

The Lake Karachai site in the South Ural has been used for storage of low-level and intermediate-level nuclear waste for decades since 1951, and contains the total activity of 1.2×10^8 Ci (Rumynin, 2011). The liquid wastes discharged into Lake Karachai contained large amounts of salts. Among them, the organic compounds dissolved in water are oxalate (expressed as $H_2C_2O_4$) and acetate (expressed as CH_3COO) with their respective concentrations of 0.9–14 g/L (0.010–0.16 mol·dm^{-3}) and 0.6–20 g/L (0.10–0.34 mol·dm^{-3}) (Rumynin, 2011). It is of interest to note that the contents of Am in the bottom sediments are 0.093 g/kg (Rumynin, 2011). The oxidation state of Am has been determined to be in +III state (Novikov et al., 2018). Therefore, it could be inferred that Am(III) may have been sequestrated as Am(III)-oxalate solid phase(s) in the bottom sediments because of the presence of high oxalate concentrations. Hence, the detailed speciation study on the bottom sediments will be important contributions to our understanding of the interactions between actinides and oxalate in a natural environments. One interesting note is that the microorganisms at the site have been found to be able to concentrate actinides (e.g., Nazina et al., 2010), and the likely mechanism is via the formation of actinide oxalates.

5.2. Interactions of oxalate with actinides in the near field of a geological repository

In certain geological repositories, there are sizable inventories of oxalate. In such geological repositories, actinide oxalates could become the solubility-controlling phases for actinides in the source term. However, as the equilibrium constants for actinide oxalates were not known before, the solubility-controlling phases for trivalent actinides such as Am(III) have been commonly assumed to be $Am(OH)_3$(s) or $AmCO_3(OH)$ (e.g., Keum et al., 2002), or $Am(OH)_3$(am) for conservatism as required by regulatory agencies. As this study has presented the solubility constants for actinide oxalates, we are in a good position to evaluate that the relative stability of actinide oxalates with respect to the proceeding inorganic phases. Here we demonstrate that trivalent actinide oxalates can be the solubility-controlling phases, i.e., source-term phases for actinides, by using $Am_2(C_2O_4)_3{\cdot}10H_2O$(cr) as an example. In the calculations below for the respective stability fields for $Am_2(C_2O_4)_3{\cdot}10H_2O$(cr), $Am(OH)_3$(s), $AmCO_3(OH)$, and $Am(OH)_3$(am), the solubility constant for $Am_2(C_2O_4)_3{\cdot}10H_2O$(cr) is from this study, that for $Am(OH)_3$(am) is from Xiong et al. (2017a), and those for $Am(OH)_3$(s) and $AmCO_3(OH)$(s) are from the EQ3/6 database contained in Domski (2015) and Xiong and Domski (2016).

As mentioned in Introduction, the repositories in the clay formations for the French nuclear waste management programs are expected to have the waste stream with oxalate (Altmann, 2008). Although the exact oxalate concentrations in the repository have not calculated, we assume that the initial oxalate concentrations range from 10^{-4} to 10^{-2} mol·kg^{-1} with a median of 10^{-3} mol·kg^{-1}. The above assumption for the oxalate concentration of 1×10^{-3} mol·kg^{-1} is reasonable, as it is supported by the following examples. In the first example, the oxalate concentrations in the WIPP, the currently only operational geological repository in the world, are computed to be 4.55×10^{-2} mol·dm^{-3} (Brush and Xiong, 2005). In the second example, as mentioned above, the oxalate concentrations in the Lake Karachai site that has been used for storage of low-level and intermediate-level liquid nuclear waste in Russia since 1951, range from 1.0×10^{-2} mol·dm^{-3} to 1.6×10^{-1} mol·dm^{-3}. Since the porewater in the Opalinus Clay formation that will host the French repositories has a low ionic strength of ~0.1 mol·kg^{-1} with low concentrations of sodium (Pearson et al., 2003, 2011), the activities of oxalate can be computed using the concentrations of oxalate and the activity coefficient for oxalate calculated based on the compositions of the solutions from Pearson et al. (2003, 2011). Fig. 13 illustrates the stability fields of $Am_2(C_2O_4)_3{\cdot}10H_2O$(cr) and $Am(OH)_3$(s) in the space of pH versus $log a_{C_2O_4^{2-}}$. In Fig. 13, the pH values for the porewater are from Pearson et al. (2003, 2011). Fig. 13 indicates that $Am_2(C_2O_4)_3{\cdot}10H_2O$(cr) instead of $Am(OH)_3$(s) is a stable phase. In addition to the stability fields at $a_{H2O} = 1$, Fig. 13 also shows the stability fields at $a_{H2O} = 0.45$. The figure suggests that the stability field of $Am_2(C_2O_4)_3{\cdot}10H_2O$(cr) with respect to $Am(OH)_3$(am). The figure suggests that $Am_2(C_2O_4)_3{\cdot}10H_2O$(cr) slightly decreases with decreasing water activity.

Fig. 14 displays the stability fields of $Am_2(C_2O_4)_3{\cdot}10H_2O$(cr) with respect to $Am(OH)_3$(am). The figure suggests that $Am_2(C_2O_4)_3{\cdot}10H_2O$(cr) has large stability fields, and should be the stable phase.

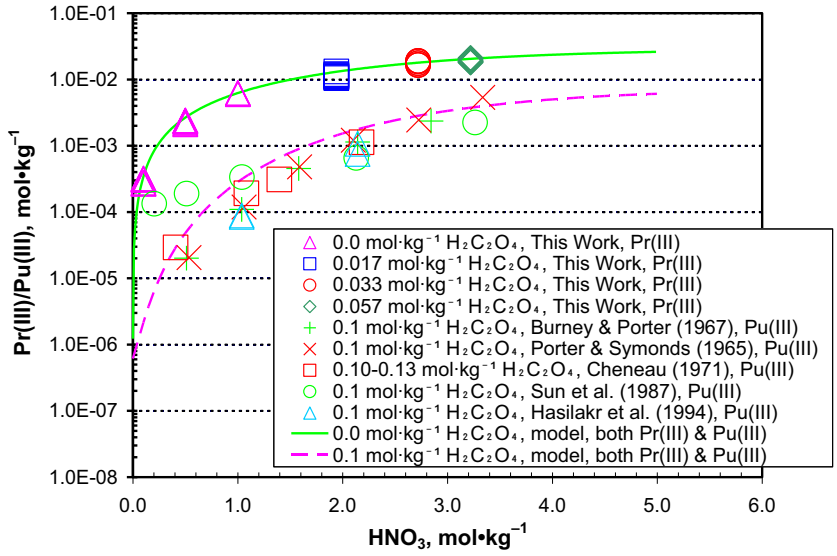


Fig. 7. A plot showing total Pr(III) or Pu(III) concentrations on a molal scale ($m_{\Sigma Pr(III)}/m_{\Sigma Pu(III)}$) in equilibrium with $Pr_2(C_2O_4)_3{\cdot}10H_2O$ or $Pu_2(C_2O_4)_3{\cdot}10H_2O$ as a function of ionic strengths with a constant concentration of oxalic acid at 0.1 mol·kg^{-1}, along with the values predicted by the model developed in this study represented by the solid and dashed lines. The solubility data for $Pu_2(C_2O_4)_3{\cdot}10H_2O$ are taken from the literature, and those literature data are not used in the model development.

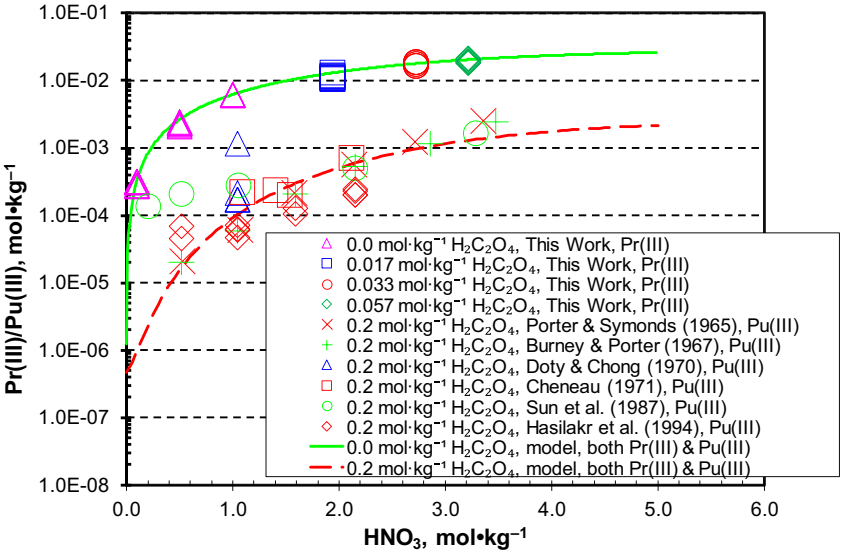


Fig. 8. A plot showing total Pr(III) or Pu(III) concentrations on a molal scale ($m_{\Sigma Pr(III)}/m_{\Sigma Pu(III)}$) in equilibrium with $Pr_2(C_2O_4)_3{\cdot}10H_2O$ or $Pu_2(C_2O_4)_3{\cdot}10H_2O$ as a function of ionic strengths with a constant concentration of oxalic acid at 0.2 mol·kg^{-1}, along with the values predicted by the model developed in this study represented by the solid and dashed lines. The solubility data for $Pu_2(C_2O_4)_3{\cdot}10H_2O$ are taken from the literature, and those literature data are not used in the model development.

Fig. 15 delineates the stability fields of $Am_2(C_2O_4)_3{\cdot}10H_2O$(cr) and $AmCO_3(OH)$(s) at various log f_{CO2} ranging from −4.5 to −2.5 bars. In those calculations, a_{H2O} is set to be 1. Notice that the log f_{CO2} for the porewater in the Opalinus Clay formation calculated from the porewater solution chemistry is about −2.5 bars. Therefore, Fig. 15 demonstrates that $Am_2(C_2O_4)_3{\cdot}10H_2O$(cr) instead of $AmCO_3(OH)$(s) should be the stable phase.

In summary, the above calculations suggest that $Am_2(C_2O_4)_3{\cdot}10H_2O$ (cr) can be a source-term phase in the near field of geological repositories in which there are organic ligands such as oxalate in the waste stream and groundwaters contain low concentrations of sodium.

It should be noted that the double salts of sodium and actinide oxalate, such as $NaYb(C_2O_4)_2{\cdot}yH_2O$ proposed by Gammons and Wood (2000), as an analog, could be the solubility-controlling phase in the environments where there are high concentrations of sodium. An example for such environments of high sodium concentrations may be the Canadian disposal of nuclear waste concept in sedimentary basins (Hobbs et al., 2008). The formation waters in sedimentary basins in the southwestern Ontario, the candidate area for the Canadian disposal concept in sedimentary basins, usually contain high concentrations of sodium (Dollar, 1988). For instance, the formation waters in the Devonian sandstone rocks have the sodium concentrations up to 4.1 mol·kg^{-1}. At such high concentrations of sodium, the double salt with the stoichiometry proposed by Gammons and Wood (2000) or with different stoichiometry may be the solubility-controlling phase for Am (III). However, this needs to be further studied.

5.3. *Interactions of oxalate with actinides in the far field of a geological repository*

Oxalate is ubiquitous at the surface of the Earth (Stephens, 2012; Gadd, 2017). When the leaked actinides from a breached repository reach the far field, they are likely to react with whewellite to form actinides oxalates. This is because whewellite is one of the most important minerals, and therefore frequently occurs, at the surface, and in the subsurface, of the Earth (Stephens, 2012; Gadd, 2017).

To quantitatively assess the interactions of actinides with oxalate in the far field, we first assume that the concentrations of the leaked actinides are controlled by the solubility of actinides, represented by Am $(OH)_3$(s) in the near field of a geological repository without organic

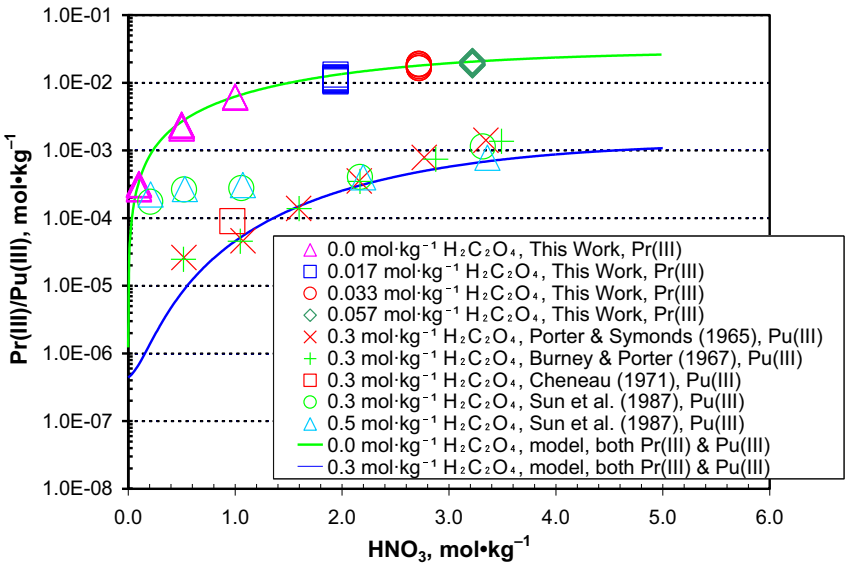


Fig. 9. A plot showing total Pr(III) or Pu(III) concentrations on a molal scale ($m_{\Sigma Pr(III)}/m_{\Sigma Pu(III)}$) in equilibrium with $Pr_2(C_2O_4)_3{\cdot}10H_2O$ or $Pu_2(C_2O_4)_3{\cdot}10H_2O$ as a function of ionic strengths with a constant concentration of oxalic acid at 0.3 mol·kg^{-1}, along with the values predicted by the model developed in this study represented by the solid lines. The solubility data for $Pu_2(C_2O_4)_3{\cdot}10H_2O$ are taken from the literature, and those literature data are not used in the model development.

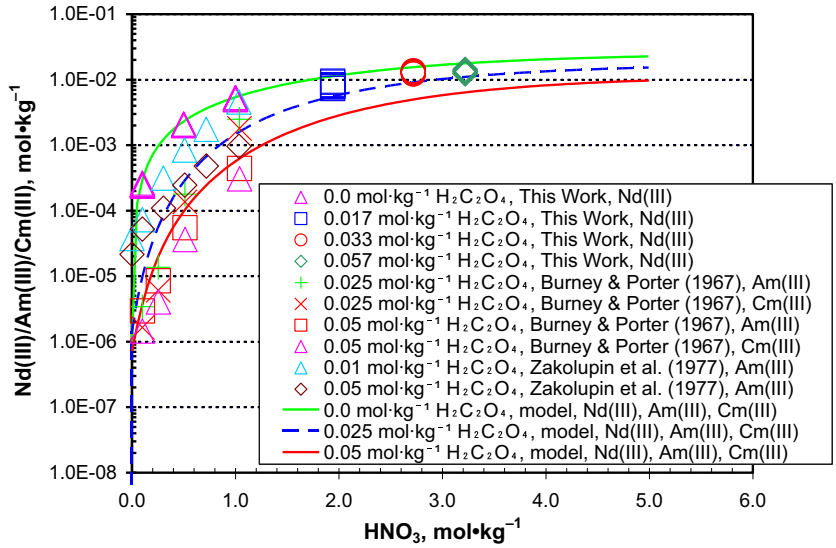


Fig. 10. A plot showing total Nd(III) or Am(III) or Cm(III) concentrations on a molal scale ($m_{\Sigma Nd(III)}/m_{\Sigma Am(III)}$ /$m_{\Sigma Cm(III)}$) in equilibrium with $Nd_2(C_2O_4)_3{\cdot}10H_2O$ or $Am_2(C_2O_4)_3{\cdot}10H_2O$ or $Cm_2(C_2O_4)_3{\cdot}10H_2O$ as a function of ionic strengths with constant concentrations of oxalic acid at 0.025 and 0.05 mol·kg^{-1}, along with the values predicted by the model developed in this study represented by the solid and dashed lines. The solubility data for $Am_2(C_2O_4)_3{\cdot}10H_2O$ and $Cm_2(C_2O_4)_3{\cdot}10H_2O$ are taken from the literature, and those literature data are not used in the model development.

ligands in the waste stream, as this phase is generally assumed to be the solubility controlling phase for actinides in +III oxidation state (e.g., Keum et al., 2002; Xiong et al., 2017a). When the repository is breached, we conservatively assume that there is no sorption. Hence the concentrations of the leaked Am(III) can be approximated by those in the near field.

Here, we use the Beishan site as an example, which is a candidate site in China for the disposal of HLW in granite (Zhou et al., 2001). In our calculations, we use the Wuyi groundwater from the Beishan site (Zhou et al., 2001) to predict the Am concentration in equilibrium with Am $(OH)_3$(s) at pH 7.5 in the near field. In the original Wuyi groundwater, the pH is 7.24 without contact with the buffer material (Zhou et al., 2001). We assume here that the pH of the groundwater slightly increases to 7.5 when it contacts with the buffer materials such as bentonite. Based on our calculations using the EQ3/6 database, DATA0.FM2 (Domski, 2015; Xiong and Domski, 2016), the Am concentration is 3.38×10^{-6} mol·kg^{-1} in the near field.

Should the above concentration of Am(III) be leaked from a breached geological repository, it would interact with whewellite and soil solutions in the far field. Regarding such interactions, we utilize the baseline soil solution (BSS) from Xiong (2009), which was modified from the soil solution of Wood (2000), to do the modeling. In the modeling, the pH of BSS is 6.5, as suggested by Wood (2000). The calculations indicate that the leaked actinides such as Am(III) precipitates as $Am_2(C_2O_4)_3{\cdot}10H_2O$ and the Am(III) concentrations decrease to 3.25×10^{-7} mol·kg^{-1} (Table 6), a decrease by one order of magnitude. This also applies to other actinides in +III oxidation state such as Pu(III) and Cm(III).

5.4. *Bio-formation of REE-oxalates, bioleaching and bio-extraction of rare earth elements*

It is of interest to note that deveroite-(Ce), a natural REE-oxalate, has recently discovered in low temperature environments (Guastoni et al., 2013). Deveroite-(Ce) has the following stoichiometry: $(Ce_{1.01}Nd_{0.33}La_{0.32}Pr_{0.11}Y_{0.11}Sm_{0.01}Pb_{0.04}U_{0.03}Th_{0.01}Ca_{0.04})_{2.01}(C_2O_4)_{2.99}{\cdot}9.99H_2O$ (Guastoni et al., 2013). Notice that deveroite-(Ce) contains both Nd(III) and Pr(III), and it can be considered as a solid solution.

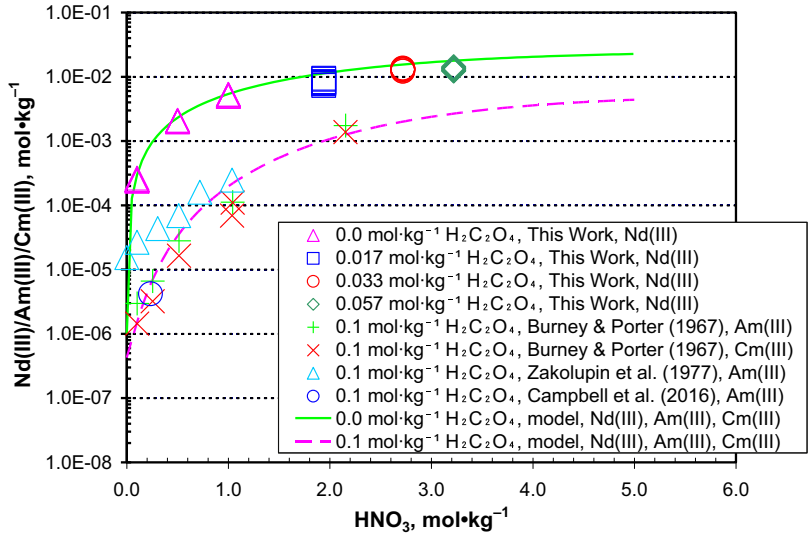


Fig. 11. A plot showing total Nd(III) or Am(III) or Cm(III) concentrations on a molal scale ($m_{\Sigma Nd(III)}/m_{\Sigma Am(III)}$ /$m_{\Sigma Cm(III)}$) in equilibrium with $Nd_2(C_2O_4)_3{\cdot}10H_2O$ or $Am_2(C_2O_4)_3{\cdot}10H_2O$ or $Cm_2(C_2O_4)_3{\cdot}10H_2O$ as a function of ionic strengths with a constant concentration of oxalic acid at 0.1 mol·kg^{-1}, along with the values predicted by the model developed in this study represented by the solid and dashed lines. The solubility data for $Am_2(C_2O_4)_3{\cdot}10H_2O$ and $Cm_2(C_2O_4)_3{\cdot}10H_2O$ are taken from the literature, and those literature data are not used in the model development.

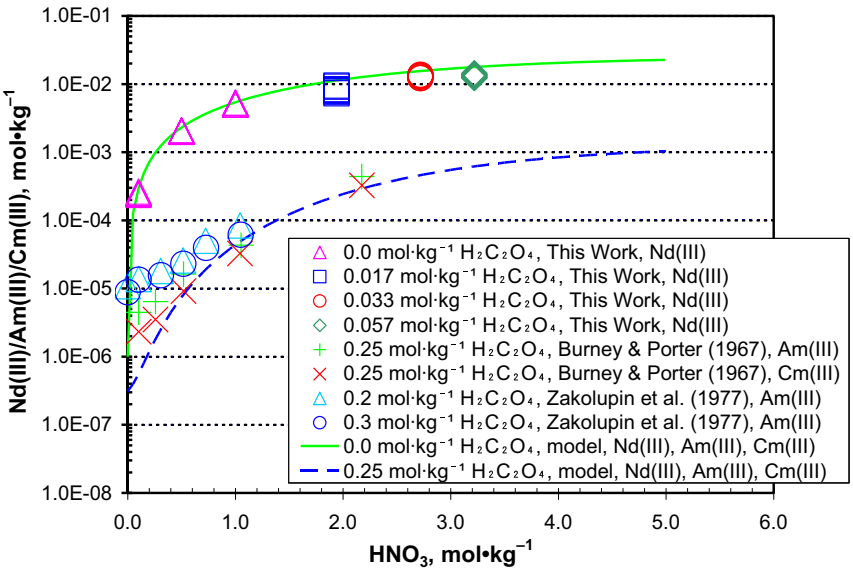


Fig. 12. A plot showing total Nd(III) or Am(III) or Cm(III) concentrations on a molal scale ($m_{\Sigma Nd(III)}/m_{\Sigma Am(III)}$ /$m_{\Sigma Cm(III)}$) in equilibrium with $Nd_2(C_2O_4)_3{\cdot}10H_2O$ or $Am_2(C_2O_4)_3{\cdot}10H_2O$ or $Cm_2(C_2O_4)_3{\cdot}10H_2O$ as a function of ionic strengths with a constant concentration of oxalic acid at 0.25 mol·kg^{-1}, along with the values predicted by the model developed in this study represented by the solid and dashed lines. The solubility data for $Am_2(C_2O_4)_3{\cdot}10H_2O$ and $Cm_2(C_2O_4)_3{\cdot}10H_2O$ are taken from the literature, and those literature data are not used in the model development.

Therefore, $Pr_2(C_2O_4)_3{\cdot}10H_2O$ and $Nd_2(C_2O_4)_3{\cdot}10H_2O$ studied in this work can be regarded as the pure Pr and Nd end-members of deveroite. The formation of deveroite has been suggested to have occurred by circulation of meteoric waters at low temperatures between 20 °C and 30 °C (Guastoni et al., 2013). REE have been leached from pegmatite dykes in Devero Valley in Italy, and the source of oxalate is via the incomplete oxidation of organic material such as decaying plant remains (e.g., crusty lichens) (Guastoni et al., 2013). The solubility constants for $Pr_2(C_2O_4)_3{\cdot}10H_2O$ and $Nd_2(C_2O_4)_3{\cdot}10H_2O$ obtained in our work can provide the further details and mechanism for the formation of deveroite, for instance, constraining the minimum REE concentrations leached from pegmatite dykes and minimum oxalate concentrations supplied by decaying organic materials.

Recent studies have demonstrated that the geoactive fungi, *Aspergillus niger*, can behave as a bio-leaching agent for REE (Kang et al., 2019, 2020; Castro et al., 2020; Mendes et al., 2020). The concentrations of REE leached by *Aspergillus niger* are up to 1.37 ppm (Castro et al., 2020). During this process, REE oxalates are precipitated. The already observed precipitates are $La_2(C_2O_4)_3{\cdot}10H_2O$ and $Ce_2(C_2O_4)_3{\cdot}10H_2O$ (Kang et al., 2019, 2020). These REE oxalates are isostructural with $Pr_2(C_2O_4)_3{\cdot}10H_2O$ and $Nd_2(C_2O_4)_3{\cdot}10H_2O$ studied by this work. Waste repositories such as mining waste are now considered as "resource hubs" for future recovery (Sapsford et al., 2017). Therefore, based on the thermodynamic properties for $Pr_2(C_2O_4)_3{\cdot}10H_2O$ and $Nd_2(C_2O_4)_3{\cdot}10H_2O$ determined by this study, the extraction of REE from "resource hubs" utilizing bioleaching with *Aspergillus niger* as an agent can be optimized in the future.

6. Conclusions

In this study, we have performed the well constrained solubility measurements on $Pr_2(C_2O_4)_3{\cdot}10H_2O$ and $Nd_2(C_2O_4)_3{\cdot}10H_2O$ to high ionic strengths. Based on our experimental data, we have developed a thermodynamic model to describe solubilities of $Pr_2(C_2O_4)_3{\cdot}10H_2O$ and

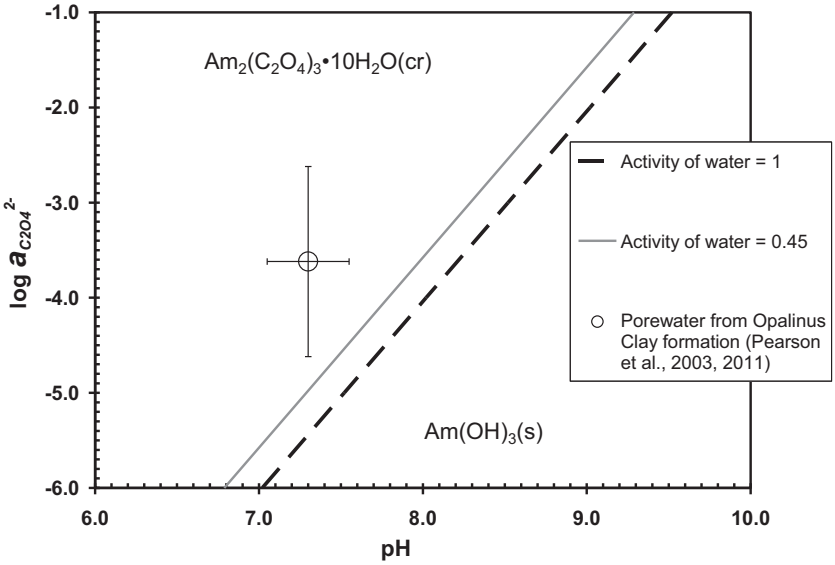


Fig. 13. The stability fields of $Am_2(C_2O_4)_3{\cdot}10H_2O$(cr) and $Am(OH)_3$(s) in the space of pH versus $loga_{C_2O_4^{2-}}$ at $a_{H2O} = 1$ and $a_{H2O} = 0.45$. The activity of oxalate is calculated based on the activity coefficient of 0.24 for oxalate and the assumed oxalate concentrations. The activity coefficient of oxalate is computed according to the ionic strength of the porewater from the Opalinus clay formation. The above notations also apply to Figs. 14 and 15.

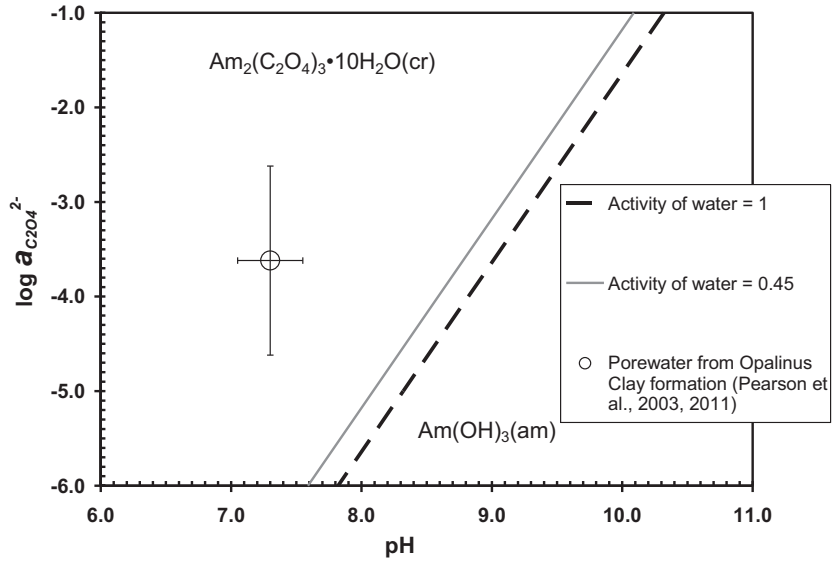


Fig. 14. The stability fields of $Am_2(C_2O_4)_3{\cdot}10H_2O$(cr) and $Am(OH)_3$(am) in the space of pH versus $loga_{C_2O_4^{2-}}$ at $a_{H2O} = 1$ and $a_{H2O} = 0.45$.

$Nd_2(C_2O_4)_3{\cdot}10H_2O$ to high ionic strengths. The calculations according to the solubility constant for $Pr_2(C_2O_4)_3{\cdot}10H_2O$ from our model reproduce well the solubility data of $Pu_2(C_2O_4)_3{\cdot}10H_2O$ from the literature, demonstrating that Pr(III) is an excellent analog to Pu(III). Similarly, the calculations based on the solubility constant for $Nd_2(C_2O_4)_3{\cdot}10H_2O$ in our model also reproduce well the solubility data of $Am_2(C_2O_4)_3{\cdot}10H_2O$ and $Cm_2(C_2O_4)_3{\cdot}10H_2O$ in the mixtures of HNO_3 and $H_2C_2O_4$ from the literature, suggesting that Nd(III) is a good analog to both Am(III) and Cm(III). Therefore, our model can be extended with high confidence to Pu(III)-, Am(III)-, and Cm(III)-oxalates, the important nuclear materials, to high ionic strengths, which is currently lacking. It is expected that our model will find applications in numerous fields, including separation of actinides in reprocessing spent nuclear fuel, decontamination of nuclear facilities, and prediction of actinide solubilities in the source term for geological repositories in the near field. The model can also be used for predictions of the interactions of the leaked actinides with geological media in the far field of a geological repository where oxalate such as whewellite is ubiquitous.

Declaration of Competing Interest

The authors declare that they have no competing financial interests or personal relationships to influence the work reported in this paper.

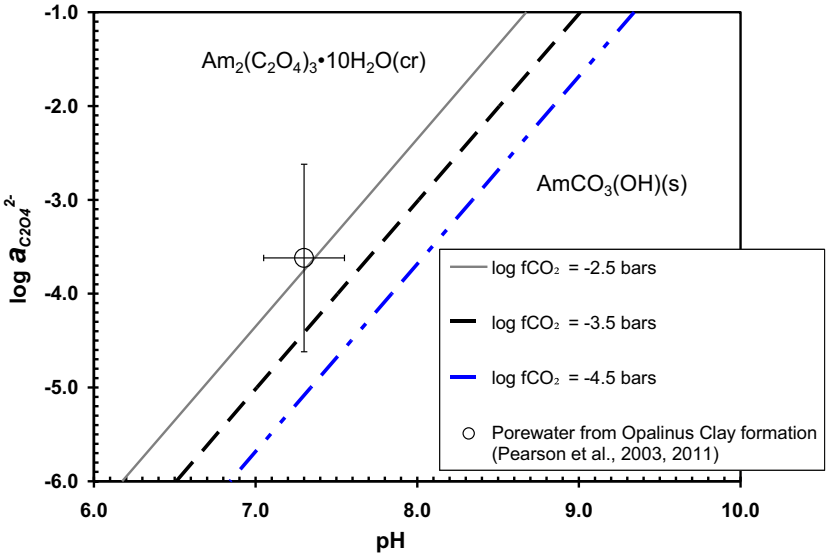


Fig. 15. The stability fields of $Am_2(C_2O_4)_3{\cdot}10H_2O$(cr) and $AmCO_3(OH)_3$(s) in the space of pH versus $log a_{C_2O_4^{2-}}$ at $log f_{CO_2} = -2.5$, $log f_{CO_2} = -3.5$, and $log f_{CO_2} = -4.5$, assuming $a_{H2O} = 1$.

Table 6
The predicted interactions of the leaked actinides represented by Am(III) with the baseline soil solution (BSS) in the far field of a geological repository.[a]

Species/parameter	Concentration, mol·kg^{-1}	Remarks
Total Am(III)	3.38×10^{-6}	The leaked actinide concentrations from a breached geological repository
$AmC_2O_4^+$	1.98×10^{-7}	After the interactions with the BSS in the far field
$Am(C_2O_4)_2^-$	1.11×10^{-7}	
Am^{3+}	7.75×10^{-9}	
$AmCO_3^+$	7.72×10^{-9}	
Ca^{2+}	1.24×10^{-4}	
CaC_2O_4(aq)	1.10×10^{-5}	
Mg^{2+}	9.02×10^{-6}	
MgC_2O_4(aq)	8.03×10^{-7}	
$MgSO_4$(aq)	1.71×10^{-7}	
Na^+	1.85×10^{-5}	
K^+	1.00×10^{-4}	
Cl^-	1.00×10^{-5}	
SO_4^{2-}	9.98×10^{-5}	
HCO_3^-	6.27×10^{-5}	
CO_2(aq)	3.73×10^{-5}	
pH	6.5	
Whewellite, $CaC_2O_4{\cdot}H_2O$(cr)	Saturated	
$Am_2(C_2O_4)_3{\cdot}10H_2O$	Saturated	

[a] The chemical compositions of the BSS before the reaction with the leaked Am(III) are taken from Xiong (2009), which in turn was modified from the formulation by Wood (2000).

Acknowledgments

Sandia National Laboratories is a multimission laboratory operated by National Technology and Engineering Solutions of Sandia, LLC., a wholly owned subsidiary of Honeywell International, Inc., for the U.S. Department of Energy's National Nuclear Security Administration under contract DE-NA-0003525. This research is funded by the Spent Fuel and Waste Science and Technology (SFWST) programs administered by the Office of Nuclear Energy (NE) of the U.S. Department of Energy. This paper is published with the release number, SAND2021-3458J. This paper describes objective technical results and analysis. Any subjective views or opinions that might be expressed in the paper do not necessarily represent the views of the U.S. Department of Energy or the United States Government. We thank Ricardo Rosa, Phil Faltas, and Sara Russo for the laboratory assistance. We are grateful to three journal reviewers for their insightful reviews. Their reviews have substantially helped to improve our presentation. We thank the Editor, Dr. Karen Johannesson, for her time and editorial efforts.

Appendix A. Comparison of major peaks in terms of Miller index in the XRD pattern of $Pr_2(C_2O_4)_3{\cdot}10H_2O$ synthesized in this study with the standard represented by PDF-00-020-0964[a]

$Pr_2(C_2O_4)_3{\cdot}10H_2O$ standard, PDF-00-020-0964			$Pr_2(C_2O_4)_3{\cdot}10H_2O$, synthized in this study		
hkl	d-Spacing, Å	Intensity	hkl	d-Spacing, Å	Intensity[b]
(100)	10.4	70	(100)	10.4	182

(continued on next page)

(*continued*)

$Pr_2(C_2O_4)_3{\cdot}10H_2O$ standard, PDF-00-020-0964			$Pr_2(C_2O_4)_3{\cdot}10H_2O$, synthized in this study		
hkl	d-Spacing, Å	Intensity	hkl	d-Spacing, Å	Intensity[b]
(110)	7.09	40	(110)	7.07	115
(11)	6.65	100	($\bar{1}$11)	6.65	353
(111)	5.01	100	(111)	5.01	233
($\bar{2}$11)	4.84	100	($\bar{2}$11)	4.84	181
($\bar{1}$22)	3.53	55	($\bar{1}$22)	3.53	140
($\bar{2}$04)	2.582	40	($\bar{2}$04)	2.582	276

[a] The major peaks with intensity ≥40 in the standard are compared with those in the synthetic $Pr_2(C_2O_4)_3{\cdot}10H_2O$. The significant numbers for d-spacing are exactly the same as present in the PDF database.
[b] Experimental relative intensity.

Appendix B. Comparison of major peaks in terms of Miller index in the XRD pattern of $Nd_2(C_2O_4)_3{\cdot}10H_2O$ synthesized in this study with the standard represented by PDF-00-020-0764[a]

$Nd_2(C_2O_4)_3{\cdot}10H_2O$ standard, PDF-00-020-0764			$Nd_2(C_2O_4)_3{\cdot}10H_2O$, synthized in this study		
hkl	d-Spacing, Å	Intensity	hkl	d-Spacing, Å	Intensity[b]
(100)	10.2	80	(100)	10.2	259
(110)	6.97	50	(110)	6.97	181
(011)	6.66	100	(011)	6.64	472
($\bar{1}$11)	6.51	100	($\bar{1}$11)	6.50	644
($\bar{1}$02)	5.11	80	($\bar{1}$02)	5.11	189
(111)	4.95	100	(111)	4.94	504
($\bar{2}$11)	4.77	100	($\bar{2}$11)	4.76	1005
($\bar{3}$02)	3.52	80	($\bar{3}$02)	3.52	158
(311)	2.725	100	(311)	2.724	218
(023)	2.614	100	(023)	2.614	182

[a] The major peaks with intensity ≥50 in the standard are compared with those in the synthetic $Nd_2(C_2O_4)_3{\cdot}10H_2O$. The significant numbers for d-spacing are exactly the same as present in the PDF database.
[b] Experimental relative intensity.

References

Akatsu, J., 1982. Separation of Pu-Am from an aqueous waste by successive oxalate and lead oxalate precipitations. Sep. Sci. Technol. 17, 1433–1442.

Altmann, S., 2008. Geo'chemical research: a key building block for nuclear waste disposal safety cases. J. Contam. Hydrol. 102 (3–4), 174–179.

Arab-Chapelet, B., Grandjean, S., Nowogrocki, G., Abraham, F., 2007. Synthesis of new mixed actinides oxalates as precursors of actinides oxide solid solutions. J. Alloys Compd. 444, 387–390.

Brunel, B., Philippini, V., Mendes, M., Aupiais, J., 2015. Actinide oxalate complexes formation as a function of temperature by capillary electrophoresis coupled with inductively coupled plasma mass spectrometry. Radiochim. Acta 103 (1), 27–37.

Brush, L.H., Xiong, Y.-L., 2005. Calculation of Actinide Solubilities for the WIPP Performance-assessment Baseline Calculations, Analysis Plan AP-120, Rev. 0. April 4, 2005. Sandia National Laboratories, Carlsbad, NM (ERMS 539255).

Burney, G.A., Porter, J.A., 1967. Solubilities of Pu (III), Am (III), and Cm (III) oxalates. Inorg. Nucl. Chem. Lett. 3 (3), 79–85.

Campbell, C., Carrigan, C., Carrott, M., Maher, C., McLuckie, B., Mason, C., Gregson, C., Griffiths, T., Holt, J., Sarsfield, M., Taylor, R., 2016. The separation of ^{241}Am from aged plutonium dioxide for use in radioisotope power systems using the AMPPEX process. Proc. Chem. 21, 140–147.

Cantrell, K.J., Riley, R.G., 2008. Subsurface Behavior of Plutonium and Americium at Non-Hanford Sites and Relevance to Hanford. Pacific Northwest National Laboratory (PNNL-17386).

Castro, L., Blázquez, M.L., González, F., Muñoz, J.A., 2020. Bioleaching of phosphate minerals using *Aspergillus niger*: recovery of copper and rare earth elements. Metals 10 (7), 978.

Chackraburtty, D.M., 1963. X-ray evidence of plutonium (III) oxalate decahydrate. Acta Crystallogr. 16 (8), 834.

Cheneau, G., 1971. The Precipitation and Filtration of Trivalent Plutonium Oxalate (No. CEA-R—4109). CEA Centre de Production de Plutonium de Marcoule.

Choppin, G.R., Bond, A.H., Borkowski, M., Bronikowski, M.G., Chen, J.-F., Lis, S., Mizera, J., Pokrovsky, O.S., Wall, N.A., Xia, Y.-X., Moore, R.C., 2001. Waste Isolation Pilot Plant Actinide Source Term Test Program: Solubility Studies and Development of Modeling Parameters. Sandia National Laboratories Report (SAND99-0943).

Crawford, B.A., Lott, S.A., Sparks, L.D., Van Soest, G., McInroy, B., 2006. The road to recertification: WIPP TRU waste inventory. In: Proceedings of Waste Management 2006 Conference; February 26–March 2, Tucson, Arizona, WMS: Tempe, AZ, 2006.

Dmitriev, S.N., Popeko, A.G., 2015. High-power radioactive targets as one of the key problems in further development of the research program on synthesis of new superheavy elements. J. Radioanal. Nucl. Chem. 305 (3), 927–933.

Dollar, P.S., 1988. Geochemistry of formation waters, southwestern Ontario, Canada and southern Michigan, U.S.A. In: Implications for Origin and Evolution. University of Waterloo, Waterloo, Ontario, Canada.. Unpublished M.Sc. thesis.

Dollimore, D., 1987. The thermal decomposition of oxalates. A review. Thermochim. Acta 117, 331–363.

Domski, P.S., 2015. "Memo AP-173, EQ3/6 Database Update: DATA0.FM2" Memorandum to WIPP Records, October 27, 2015. Sandia National Laboratories, Carlsbad, NM (ERMS 564914).

Doty, J.W., Chong, C.H.H., 1970. Preparation of micron-sized $^{238}PuO_2$. J. Nucl. Mater. 35 (2), 247–249.

Ferri, D., Iuliano, M., Manfredi, C., Vasca, E., Caruso, T., Clemente, M., Fontanella, C., 2000. Dioxouranium (VI) oxalate complexes. J. Chem. Soc. Dalton Trans. 19, 3460–3466.

Fomina, M., Podgorsky, V.S., Olishevska, S.V., Kadoshnikov, V.M., Pisanska, I.R., Hillier, S., Gadd, G.M., 2007. Fungal deterioration of barrier concrete used in nuclear waste disposal. Geomicrobiol J. 24 (7–8), 643–653.

Gadd, G.M., 2017. Fungi, rocks, and minerals. Elements 13, 171–176.

Gadd, G.M., Bahri-Esfahani, J., Li, Q.-W., Rhee, Y.J., Wei, Z., Fomina, M., Liang, X.-J., 2014. Oxalate production by fungi: significance in geomycology, biodeterioration, and bioremediation. Fungal Biol. Rev. 28 (2–3), 36–55.

Gammons, C.H., Wood, S.A., 2000. The aqueous geochemistry of REE: part 8: Solubility of ytterbium oxalate and the stability of Yb(III)-oxalate complexes in water at 25°C to 80°C. Chem. Geol. 166 (1–2), 103–124.

Guastoni, A., Nestola, F., Gentile, P., Zorzi, F., Alvaro, M., Lanza, A., Peruzzo, L., Schiazza, M., Casati, N.M., 2013. Deveroite-(Ce): a new REE-oxalate from Ount Cervandone, Devero Valley, western-central Alps, Italy. Mineral. Mag. 77, 3019–3026.

Hasilkar, S.P., Khedkar, N.B., Chander, K., Jadhav, A.V., Jain, H.C., 1994. Studies of the solubility of Pu(III) oxalate. J. Radioanal. Nucl. Chem. 185, 119–125.

Hobbs, M.Y., Frape, S.K., Shouakar-Stash, O., Kennell, L.R., 2008. Phase I regional hydrogeochemistry, southern Ontario: OPG's Deep Geologic Repository for low & intermediate level waste. In: Supporting Technical Report OPG 00216-REP-01300-00006-R00, Ontario Power Generation, Toronto, Canada, November 30, 2008.

Hoffman, D.C., 1985. In: Edelstein, N.M., Navratil, J.D., Schulz, W.W. (Eds.), Americium and Curium Chemistry and Technology. Reidel Publishing, Boston, pp. 241–260.

Hummel, W., Anderegg, G., Puigdomenech, I., Rao, L., Tochiyama, O., 2005. Chemical Thermodynamics of Compounds and Complexes of U, Np, Pu, Am, Tc, Zr, Ni and Se with Selected Organic Ligands. Chemical Thermodynamics, vol. 9. OECD Nuclear Energy Agency, Data Bank; Elsevier B.V. Amsterdam, Issy-les-Moulineaux, France; The Netherlands, p. 1088.

Jenkins, I.L., Moore, F.H., Waterman, M.J., 1965. X-ray powder crystallographic data on plutonium and other oxalates—I: the oxalates of plutonium (III) and plutonium (VI) and their isomorphs. J. Inorg. Nucl. Chem. 27 (1), 77–80.
Kang, X., Csetenyi, L., Gadd, G.M., 2019. Biotransformation of lanthanum by *Aspergillus niger*. Appl. Microbiol. Biotechnol. 103 (2), 981–993.
Kang, X., Csetenyi, L., Gadd, G.M., 2020. Monazite transformation into Ce-and La-containing oxalates by *Aspergillus niger*. Environ. Microbiol. 22 (4), 1635–1648.
Kettler, R.M., Palmer, D.A., Wesolowski, D.J., 1991. Dissociation quotients of oxalic acid in aqueous sodium chloride media to 175°C. J. Solut. Chem. 20 (9), 905–927.
Kettler, R.M., Wesolowski, D.J., Palmer, D.A., 1998. Dissociation constants of oxalic acid in aqueous sodium chloride and sodium trifluoromethanesulfonate media to 175°C. J. Chem. Eng. Data 43 (3), 337–350.
Keum, D.-K., Baik, M.-H., Hahn, P.-S., 2002. Speciation and solubility of major actinides under the deep groundwater conditions of Korea. J. Korean Nucl. Soc. 34, 517–531.
Krivokhatsky, A., Dubasov, Y., Smirnova, E., Skovorodkin, N., Savonenkov, V., Alexandrov, B., Lebedev, E., 1991. Actinides in the near release from the Chernobyl NPP accident. J. Radioanal. Nucl. Chem. 147 (1), 141–151.
Leighton, W.G., Forbes, G.S., 1930. Precision actinometry with uranyl oxalate. J. Am. Chem. Soc. 52 (8), 3139–3152.
Lobanov, Y.V., Buklanov, G.V., Abdullin, F.S., Polyakov, A.N., Shirokovsky, I.V., Tsyganov, Y.S., Utyonkov, V.K., 1997. Targets of uranium, plutonium, and curium for heavy-element research. Nucl. Instrum. Meth. Phys. Res. A 397 (1), 26–29.
Lujaniene, G., Plukis, A., Kimtys, E., Remeikis, V., Jankünaite, D., Ogorodnikov, B.I., 2002. Study of ^{137}Cs, ^{90}Sr, ^{239,240}Pu, ^{238}Pu and ^{241}Am behavior in the Chernobyl soil. J. Radioanal. Nucl. Chem. 251 (1), 59–68.
Lumetta, G.J., Thompson, M.C., Penneman, R.A., Eller, P.G., 2008. Curium. In: The Chemistry of the Actinide and Transactinide Elements. Springer, Dordrecht, pp. 1397–1443.
MacGowan, D.B., Surdam, R.C., 1988. Difunctional carboxylic acid anions in oilfield waters. Org. Geochem. 12 (3), 245–259.
MacGowan, D.B., Surdam, R.C., 1990. Carboxylic acid anions in formation waters, San Joaquin Basin and Louisiana Gulf Coast, USA—implications for clastic diagenesis. Appl. Geochem. 5 (5–6), 687–701.
Machuron-Mandard, X., Madic, C., 1996. Plutonium dioxide particle properties as a function of calcination temperature. J. Alloys Compd. 235 (2), 216–224.
Markin, T.L., 1958. The thermal decomposition of americium (III) oxalate. J. Inorg. Nucl. Chem. 7, 290–291.
Marsac, R., Réal, F., Banik, N.L., Pédrot, M., Pourret, O., Vallet, 2017a. Aqueous chemistry of Ce(IV): estimations using actinide analogues. Dalton Trans. 46 (39), 13553–13561.
Marsac, R., Banik, N.L., Lutzenkirchen, J., Catrouillet, C., Marquardt, C.M., Johannesson, K.H., 2017b. Modeling metal ion-humic substances complexation in highly saline conditions. Appl. Geochem. 79, 52–64.
Mendes, G.D.O., Bahri-Esfahani, J., Csetenyi, L., Hillier, S., George, T.S., Gadd, G.M., 2020. Chemical and physical mechanisms of fungal bioweathering of rock phosphate. Geomicrobiol. J. 1–11.
Nazina, T.N., Luk'yanova, E.A., Zakharova, E.V., Konstantinova, L.I., Kalmykov, S.N., Poltaraus, A.B., Zubkov, A.A., 2010. Microorganisms in a disposal site for liquid radioactive wastes and their influence on radionuclides. Geomicrobiol J. 27 (5), 473–486.
Novikov, A.P., Vlasova, I.E., Safonov, A.V., Ermolaev, V.M., Zakharova, E.V., Kalmykov, St N., 2018. Speciation of actinides in groundwater samples collected near deep nuclear waste repositories. J. Environ. Radioact. 192, 334–341.
Porter, J.A., Symonds Jr., A.E., 1965. Precipitation of Plutonium (III) Oxalate and Calcination to Plutonium Dioxide (No. DP-981). Du Pont de Nemours (EI) and Co, Aiken, SC Savannah River Lab.
Rumynin, V.G., 2011. Chapter 15. Radioactive brine migration at the Lake Karachai site (South Urals, Russian Federation). In: Subsurface Solute Transport Models and Case Histories. Springer, Dordrecht, pp. 495–518.
Sapsford, D., Cleall, P., Harbottle, M., 2017. In situ resource recovery from waste repositories: exploring the potential for mobilization and capture of metals from Anthropogenic ores. J. Sustain. Metal. 3 (2), 375–392.
Sarsfield, M.J., 2015. The coprecipitation and conversion of mixed actinide oxalates for aqueous-based reprocessing of spent nuclear fuels. In: Reprocessing and Recycling of Spent Nuclear Fuel, pp. 325–351.
Scherer, V., Fochler, M., 1968. The thermal decomposition of curium (III) oxalate IO-hydrate. J. Inorg. Nucl. Chem. 30 (6), 1433–1437.
Shannon, R.D., 1976. Revised effective ionic radii and systematic studies of interatomic distances in halides and chalcogenides. Acta Crystallogr. Sect. A: Cryst. Phys., Diffr., Theor. Gen. Crystallogr. 32 (5), 751–767.
Solodov, I.N., Velichkin, V.I., Zotov, A.V., Kochkin, B.T., Drozhko, E.G., Glagdolev, A.V., Skokov, A.N., 1994. Distribution and Geochemistry of Contaminated Subsurface Waters in Fissured Volcanogenic Bed Rocks of the Lake Karachai area, Chelyabinsk, Southern Urals. Lawrence Berkeley Laboratory Report Series, Berkeley (LBL-36780, UC-603).
Stephens, W.E., 2012. Whewellite and its key role in living system. Geol. Today 28, 180–185.
Sun, Z., Hu, H., Xue, S., Qing, Z., 1987. The solubility of Pu(III) oxalate. Atom. Energy Sci. Technol. 21, 326–329.
Thakur, P., Xiong, Y.-L., Borkowski, M., 2015. Improved thermodynamic model for the complexation of trivalent actinides and lanthanide with oxalic acid to high ionic strength. Chem. Geol. 413, 7–17.
Tsyganov, Y.S., 2014. Synthesis of new superheavy elements using the Dubna Gas-Filled Separator: the complex of technologies. Phys. Part. Nucl. 45 (5), 817–847.
Weigel, F., Ter Meer, N., 1967. The unit cells of some americium (III)—salts with organic anions. Inorg. Nucl. Chem. Lett. 3, 403–408.
Wolery, T.J., Xiong, Y.-L., Long, J., 2010. Verification and Validation Plan/Validation Document for EQ3/6 Version 8.0a for Actinide Chemistry, Document Version 8.10. Sandia National Laboratories, Carlsbad, NM (ERMS 550239).
Wood, S.A., 2000. In: Giordano, T.H., Kettler, R.M., Wood, S.A. (Eds.), Ore Genesis and Exploration: The Roles of Organic Matter. Reviews in Economic Geology, vol. 9. Society of Economic Geologist, Littleton, Colorado, pp. 157–192.
Xiong, Y.-L., 2009. The aqueous geochemistry of thallium: speciation and solubility of thallium in low temperature systems. Environ. Chem. 6, 441–451.
Xiong, Y.-L., 2011a. WIPP Verification and Validation Plan/Validation Document for EQ3/6 Version 8.0a for Actinide Chemistry, Revision 1, Document Version 8.20. Supersedes ERMS 550239. Sandia National Laboratories, Carlsbad, NM (ERMS 555358).
Xiong, Y.-L., 2011b. Release of EQ3/6 Database DATA0.FM1. Sandia National Laboratories, Carlsbad, NM (ERMS 555152, and the associated document, ERMS 555154).
Xiong, Y.-L., 2011c. Organic species of lanthanum in natural environments: implications to mobility of rare earth elements in low temperature environments. Appl. Geochem. 26 (7), 1130–1137.
Xiong, Y., 2015. Experimental determination of lead carbonate solubility at high ionic strengths: a Pitzer model description. Chem. Month. 146 (9), 1433–1443.
Xiong, Y.-L., 2018. Corrigendum to "Experimental determination of solubilities of di-calcium ethylenediaminetetraacetic acid hydrate [$Ca_2C_{10}H_{12}N_2O_8{\cdot}7H_2O$(s)] in NaCl and $MgCl_2$ solutions to high ionic strengths and its Pitzer model: Applications to geological disposal of nuclear waste and other low temperature environments". Chem. Geol. 493, 567–568.
Xiong, Y.-L., Domski, P.S., 2016. Updating the WIPP Thermodynamic Database, Revision 1, Supersedes ERMS 565730. Sandia National Laboratories, Carlsbad, NM (ERMS 566047).
Xiong, Y., Kirkes, L., Marrs, C., 2017a. Long-term experimental determination of solubilities of micro-crystalline Nd (III) hydroxide in high ionic strength solutions: applications to nuclear waste management. Aquat. Geochem. 23, 359–375.
Xiong, Y., Kirkes, L., Westfall, T., 2017b. Experimental determination of solubilities of di-calcium ethylenediaminetetraacetic acid hydrate [$Ca_2C_{10}H_{12}N_2O_8{\cdot}7H_2O$(s)] in NaCl and $MgCl_2$ solutions to high ionic strengths and its Pitzer model: applications to geological disposal of nuclear waste and other low temperature environments. Chem. Geol. 454, 15–24.
Zakolupin, S.A., Korablin, E.V., 1977. On the americium oxalate solubility. Radiokhimiya 19 (5), 698–701.
Zhdanova, N., Fomina, M., Redchitz, T., Olsson, S., 2000. Chermobyl effects: growth characteristics of soil fungi Cladosprorium cladosporiodes (Fresen) de Vries with and without positive radiotropism. Pol. J. Ecol. 49, 309–318.
Zhou, W.-B., Zhang, Z.-S., Li, M.-G., 2001. Modeling of water-glass and water-granite interaction in Beishan Area, Northwestern China. Nucl. Backend Res. 7, 85–90.